Volatiles Around Two Dimensional Defect Structures As Indicated By Micro Diamonds In Decompression Cracks

by

Jessika Potgieter

Dissertation submitted in fulfilment of the requirements for the degree of

MAGISTER SCIENTIAE

in the Faculty of Natural and Agricultural Science

Department of Geology

University of the Free State

Bloemfontein

South Africa

May 2011

Supervisor: Dr Holger Sommer

Declaration

I declare that the dissertation hereby handed in for the qualification Magister Scientiae at the University of the Free State is my own independent work and that I have not previously submitted the same work for a qualification at another University or faculty.

Signed at Bloemfontein on the ___ day of _____ 2011.

_____

Jessika Potgieter

Abstract

New evidence exist that micro diamonds do not only form at high pressure and under high temperature conditions in the diamond window, but can also be synthesized by polycondensation of light carbon-bearing molecules at medium to low pressure conditions under favourable thermodynamic, stoichiometric and kinetic circumstances. This process may even occur close to the Earth´s surface. The studied eclogites contain OH, CO_2, CO, CH_4, CH_2O and CH_3OH. These C:O:H-bearing volatiles can be found around totally embedded micro cracks in nominally anhydrous minerals (NAMS). Micro cracks act like monomineralic and interphase grain boundaries, and can also be interpreted as two dimensional defect structures.

High-resolution synchrotron based FT-IR was used in the study to detect C:O:H-bearing volatiles around two-dimensional defect structures in NAMS; for example garnet. A correlation between the different C:O:H-bearing volatiles is visible in the micro diamond bearing defect structures, whereas in inclusion free defect structures, no correlation of the different C:O:H containing volatiles can be recognized. The findings from the study shows that the C:O:H-bearing volatiles, and their distribution pattern around the studied micro cracks, are indicators for the formation of micro diamonds in natural eclogites. The outcomes confirm the results from experimental studies on the growth and synthesis of diamond crystals as a consequence of polycondensation of light carbon molecules.

Content

List of Figures

Chapter 1: Diamonds, Kimberlites and Xenoliths

1.1 Geotectonic Setting of Diamond Deposits

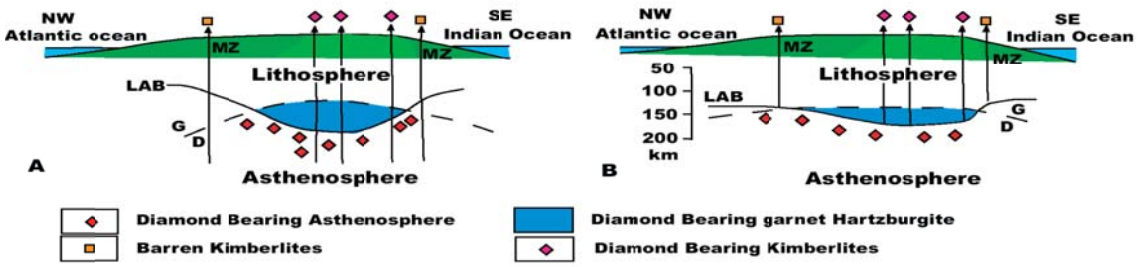

Figure 1. Contrasting models showing barren and diamond-rich kimberlites. (Mitchell, 1995, Boyd and Gurney 1986).

Diamondiferous kimberlites are most commonly found in Precambrian cratons especially in those of an Archaean age. Kimberlites can range in age from late Archaean to cainozoic and are thus formed over the entire time scale of the earth's history. Kimberlites are cratonic, whereas lamproites occur in cratonized accreted mobile belts in regions of thickened continental crust (40-55 km) and lithosphere (150-250 km) (Mitchell, 1986, 1995).

Diamonds are formed in relatively cool continental roots. The distribution of indicator minerals on the Kaapvaal craton in South Africa clearly shows the occurrence of diamond-bearing kimberlites located within the Archaean craton. Kimberlites outside of the craton are not diamond bearing, which demonstrates that below the Kaapvaal craton the lithosphere is in the garnet peridotite stability field where diamonds can be formed.

Figure 1 shows contrasting models illustrating why diamond-bearing kimberlites are restricted to within the bounds of the Kaapvaal craton and barren kimberlites are confined to adjacent mobile belts. (A) In the Haggerty (1986) and Mitchell (1995) model, kimberlites are derived from similar depths within the asthenosphere as a result of partial melting of upwelling material. Asthenospheric diamonds are formed by methane dissociation at the lithosphere-asthenosphere boundary (LAB) in the vicinity of the deepest parts of the craton root (Haggerty, 1986). Lithospheric diamonds occur only within the harzburgitic root of the craton. Only kimberlites which pass through this region can entrain xenocrystal diamonds. (B) In the Boyd and Gurney (1986) model, kimberlites are derived from different depths at the lithosphere-asthenosphere boundary, the location of which is defined by the equilibration

parameters of garnet lherzolite xenoliths found in kimberlites. In the mobile belts the boundary is considered to lie within the graphite stability field. Diamonds are believed to be stable only within the deepest part of the craton root. In this model all diamonds are of lithospheric origin.

1.2 Kimberlites and Lamproites

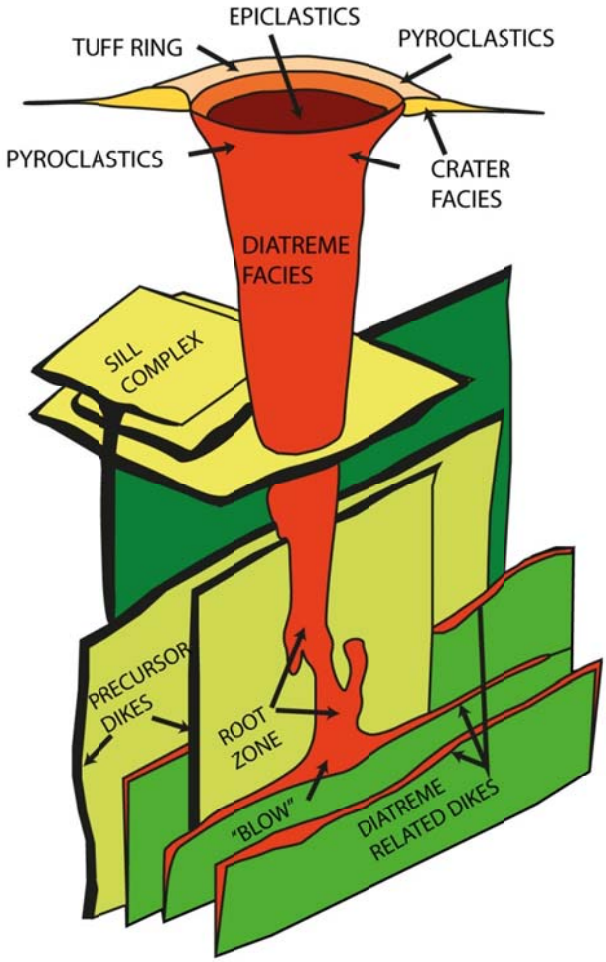

Figure 2. Kimberlite pipe deposit model (Sheahan and Cherry., 1993)

Two types of kimberlites can be found:

Type 1 kimberlite is an olivine-monticellite-serpentine-kimberlite. It shows macrocrystals of Mg-rich ilmenite and Cr-poor Ti-pyrope. The Sm/Nd isotope ratios are close to those of the bulk earth, which is suggestive of the formation of type 1 kimberlite in the asthenosphere (Sheahan and Cherry, 1993).

Type 2 kimberlite is a mica-kimberlite, or so-called “orangeite” which can only be found in South Africa. They contain Al-rich diopside, micas and Ba-K-V-Titanites. The Sm/Nd isotope ratios pinpoint the formation of type 2 kimberlites in the lithosphere (Sheahan and Cherry, 1993).

Type 1 kimberlites are more CO_2-rich, whereas type 2 kimberlites are more H_2O-rich and therefore type 2 kimberlites shows a higher fO_2 (Sparks et al., 2006). In general kimberlites are highly explosive extrusive rocks. These rocks travel through the lithosphere within a view hours (Sparks et al., 2006). They collect debris such as mantle xenoliths, crustal xenoliths and diamonds on their way to the surface.

The typical type 1 kimberlite can show three facies: the crater-facies, the diatreme-facies and the hypabyssic-facies (Mitchell, 1995; Sparks et al., 2006). All three complexes are about 1 km in depth. The crater-facies is mostly eroded and the formation of the facies is not yet understood. The diatreme-facies is characterized by high gas concentrations and the hypabyssic-facies shows typical magmatic fractionation processes.

Type 2 kimberlites shows nearly the same facies, but instead of the elliptical type 1 diatremes, they form thin (2m) and long (10km) fissures. Type 2 kimberlites usually form sub-parallel fissures, but only a few of them are diamond-bearing (Sheahan and Cherry, 1993).

A kimberlitic melt can be formed at low melt gradients in the upper mantle from a H_2O and CO_2 (or other C-O-H species) bearing peridotites (Mitchell, 1995). These peridotites occur as so-called phlogopite-dolomite-peridotites, phlogopite-peridotite or as dolomite-peridotite (Sommer, 2009*a*).

1.3 Kimberlite Uplift

As a kimberlite travels through the mantle the diamonds are incorporated into the kimberlitic melt. These diamonds are then carried to the surface of the earth. The survival of these diamonds depends on the fO_2 of the kimberlitic melt. If the fO_2 is too high during uplift the diamonds will be resorbed due to a reaction to CO_2. The diamonds will turn back in to graphite (Fedortchouk et al., 2005 and Fedortchouk and Canil, 2009).

The addition of small amounts of H_2O and CO_2 will cause the formation of partial melts that are rich in these compounds. This is due to a decrease in melt temperature of about 200°C (Sparks et al., 2006). These partial melts will rise adiabatically triggering the production of volatiles by the carbonate bearing kimberlitic melt. These volatiles are produced at depths of about 100 km. The volatile increase within the kimberlitic melt leads to the explosive stage of the kimberlite, which ends in an over-pressured choked flow (Sparks et al., 2006). These authors developed a 4-stage model for the emplacement of the kimberlite.

According to this model, kimberlite eruption began near the surface, originally from a fissure as a consequence of the magma being over-pressured due to its high volatile content. The original eruption produced a crater, but due to sustained over-pressure of the magma most of the erupted material was expelled from the crater (Sparks et al., 2006).

The second stage was the formation of the pipe caused by the widening and deepening of the crater, this stage was thus seen as an erosive phase. Stage 3 began when the crater widened to a critical point when the exploding mixture reached 1 atm. Past this point material was no longer ejected from the crater thus causing deposition within the pipe. If favourable conditions prevailed, fluidisation of the deposited pyroclastic materials could occur. The fluidisation was seen as a procedure that changed unconsolidated pyroclastic debris in the vent, and it was not suggested that this was the process that formed the pipe. The last stage involved post-emplacement hydrothermal metamorphism and alteration (Sparks et al., 2006).

These stages, especially stages 2 and 3, were not imagined to be simple two-stage processes, but processes that could be repeated regularly causing overlapping events of pipe widening, emptying and filling. It is therefore implied that the formation of a pipe could be a long-lived process (Sparks et al., 2006).

An alternative model is that kimberlites can move up to Rayleigh-wave speed through the continental crust. The mechanism proposed for this alternative model is “Weertman cracks”.

These cracks are two- dimensional liquid-filled fluid fractures, which may potentially be used for the migration of the kimberlitic melt from the Earth's mantle to the surface (Weertman, 1971*a/b*; Takada, 1990; Spence and Turcotte, 1990; Roper and Lister, 2007; Sommer et al., 2009*b*).

The first studies on fluid driven fractures were experiments using different liquids, water-filled crevasses in glaciers and vertical magma transport beneath ocean ridges (Weertman, 1971*a/b*). Recently, Sommer et al., 2009b gave new evidence which supports the formation of "Weertman" cracks as a possible mechanism for the supersonic ascent of kimberlitic melts into the continental lithosphere.

Field observations of peridotitic and eclogitic mantle xenoliths within kimberlites supports the theory for the formation of "Weertman" cracks. This is because the mantle xenoliths are incorporated into the kimberlite. As the kimberlite nears the earth's surface these xenoliths of up to 200kg gets stuck inside the kimberlite. This directly contradicts the previously mentioned four-stage eruption model (Sparks et al., 2006). The reason for this is that these xenoliths are found within the upper part of the kimberlite and according to the Sparks model should have been expelled in the eruption. The xenoliths were thus not expelled due to eruption processes. An extremely fast crystallization process of the kimberlitic melt is also necessary to keep the heavy xenoliths from sinking deeper within the pipe.

1.4 The Origin of Carbon

Two models exist in explaining the origin of the carbon:

1) All carbon is primordial carbon, which was concentrated in the mantle during the accretion of the earth (Melissa et al., 1995).

2) The carbon is partially from the mantle and partially re-subducted crustal carbon (organic carbon) (Melissa et al., 1995).

Carbon isotopes can be used to locate the origin of the carbon. Carbon has two stable isotopes, ^{12}C and ^{13}C. P-type diamonds show relative homogeneous C isotope values of about –5 ‰. E-type diamonds, in contrast show a significant variation in C-isotopes, indicating an inhomogeneous mantle source or a combination of sources of carbon, e.g. subduction. In general E-type diamonds are younger than P-type diamonds (Melissa et al., 1995). This is due to plate tectonic processes, which brings about the distribution of biogenic carbon in the sublithospheric mantle.

Chapter 2: Introduction

2.1 Purpose of Study

Diamonds are thought to be formed at high pressures and temperatures in the diamond window. Two types of diamonds can occur: E- and P-type. E type diamonds occur with eclogites and are formed from organic carbon, whereas P type diamonds are associated with peridotites and are formed from inorganic carbon. Resorbtion experiments on diamonds gave evidence that diamonds start to resorb within a few minutes to a couple of hours depending on the fO_2. The conclusion formed from these experiments is that uplift from the diamond-bearing host must be within 10 minutes to about 5 hours if the diamonds are formed in the Earth´s upper mantle (Fedortchouk et al., 2005 and Fedortchouk and Canil, 2009; Arima and Kozai., 2008). Rudenko et al., 1993 identified these micro diamonds within micro cracks and in late-formed serpentine veins and found in his experiments that micro diamonds can be formed at very low pressures.

The purpose of this study therefore is to find evidence for the formation of micro diamonds close to the Earth's surface. Volatile distribution around diamond-bearing and non-diamond-bearing micro cracks was studied. Furthermore micro Raman studies was used to prove that the inclusions found in the micro cracks and the serpentine veins are micro diamonds. Eclogites from the Roberts Victor mine were used for this study.

2.2 The Study Area

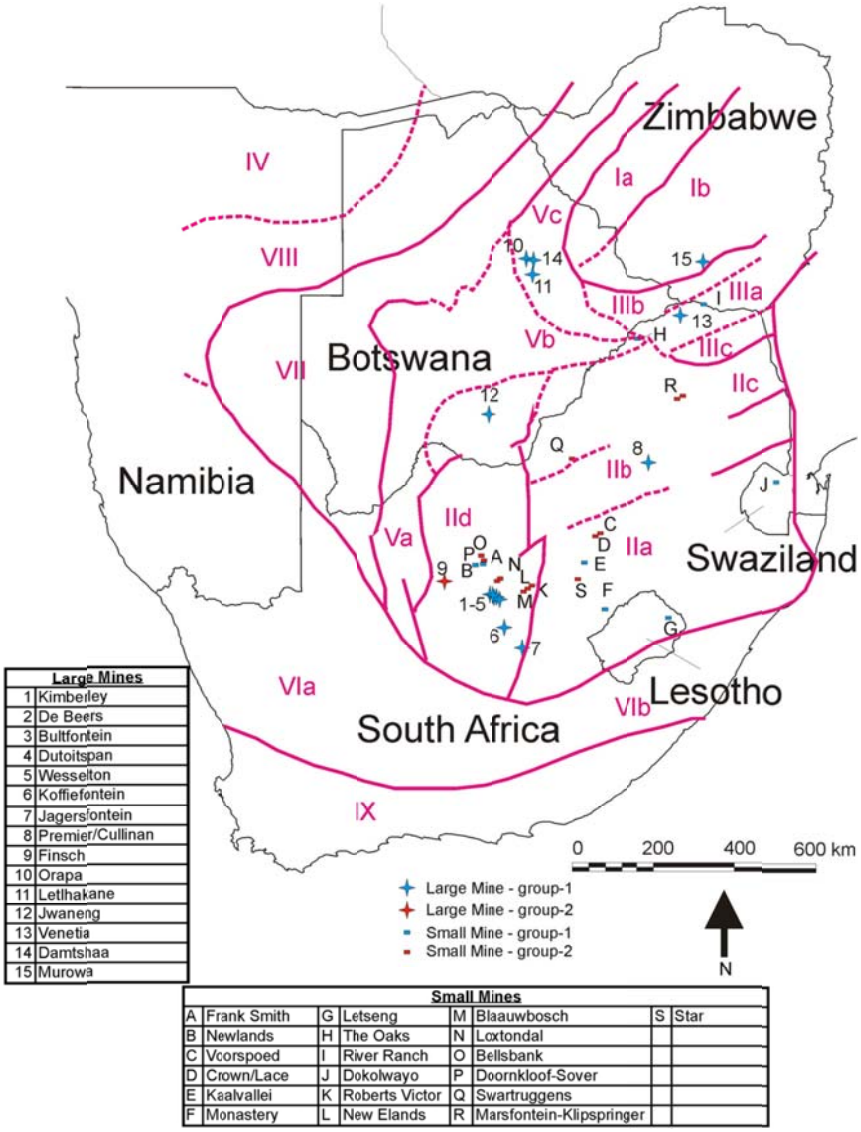

Large Mines	
1	Kimberley
2	De Beers
3	Bultfontein
4	Dutoitspan
5	Wesselton
6	Koffiefontein
7	Jagersfontein
8	Premier/Cullinan
9	Finsch
10	Orapa
11	Letlhakane
12	Jwaneng
13	Venetia
14	Damtshaa
15	Murowa

Small Mines							
A	Frank Smith	G	Letseng	M	Blaauwbosch	S	Star
B	Newlands	H	The Oaks	N	Loxtondal		
C	Voorspoed	I	River Ranch	O	Bellsbank		
D	Crown/Lace	J	Dokolwayo	P	Doornkloof-Sover		
E	Kaalvallei	K	Roberts Victor	Q	Swartruggens		
F	Monastery	L	New Elands	R	Marsfontein-Klipspringer		

Figure 3. Map showing the location of kimberlite-hosted diamond mines in southern Africa superimposed on the structural units of Griffin et al. (2003b). The structural units are: I: Archaean Zimbabwe craton; II: Archaean Kaapvaal craton; III: Archaean Limpopo micro continent; IV: Archaean Angolan craton; V: Early Proterozoic crust; VI: Early-middle Proterozoic crust — Namaqua–Natal belt; VII: Early-middle Proterozoic crust — Rehobothian subprovince; VIII: Late-Proterozoic crust — Damara province; IX: Saldanian province. The subdivisions of the structural units are: Ia: Tokwe terrain; Ib: North-western terrain; IIa: South-Eastern terrain; IIb: Central terrain; IIc: Pietersburg terrain; IId: Western terrain; IIIa: Central zone; IIIb: Northern marginal zone; IIIc: Southern marginal zone; Va: Kheis fold belt; Vb: Okwa inlier; Vc: Makondi foldbelt. The Roberts Victor mine (K) is shown as a group 2 kimberlite (Field et al., 2008)

The Roberts Victor diamond mine is situated about 40 km east of Boshof in the Free State province of South Africa. This kimberlite deposit consists of two dykes, one being associated with two small pipes (Gurney and Kirkley., 1996). The pipes contain large masses of Beaufort Sandstone as well as Karoo basalt xenoliths which were derived from above current erosion levels. Only lithic clasts from the immediate wallrock and deeper lithologies were found in the dykes. Several varieties of kimberlite have been observed in the pipe-dyke system (Wagner., 1914) and the occurrence has been classified as a Group-2 kimberlite (Fig. 3) (Skinner., 1989). The phlogopites found in the kimberlite have been dated using Rb-Sr methods resulting in two dates, namely 127±3 Ma (Allsopp and Barrett., 1975) and 128±15 Ma (Smith et al., 1985)

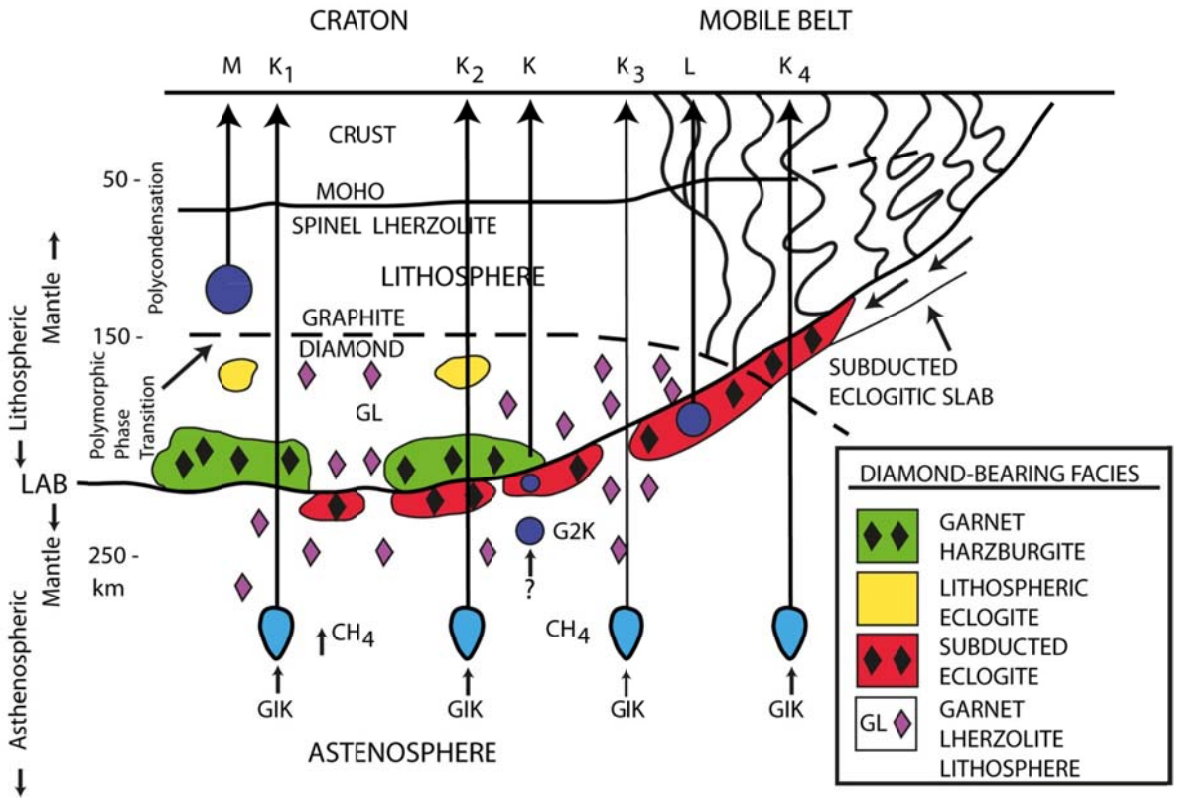

Figure 4. A schematic map of a subduction model which shows kimberlite locations hosting different xenoliths (K, K_1, K_2, K_3 and K_4) as well as lamproites (L). Different diamond-bearing xenolith (garnet lherzolite, subducted eclogite, garnet harzburgite and lithospheric eclogite) are also depicted in this model. These xenoliths are all found in the Roberts Victor mine (K2) (Sheahan and Cherry., 1993).

Roberts Victor is also a mantle xenolith-rich mine (Wagner, 1914). Four different types of diamond bearing xenoliths exist; garnet lherzolite, subducted eclogite, garnet harzburgite and lithospheric eclogites (Fig. 4). It can be seen in figure 4 that the Roberts Victor mine (K_2) contains all the above mentioned diamond-bearing xenoliths. The samples used for the purpose of this study are of subducted eclogitic composition (Melissa et al., 1995)

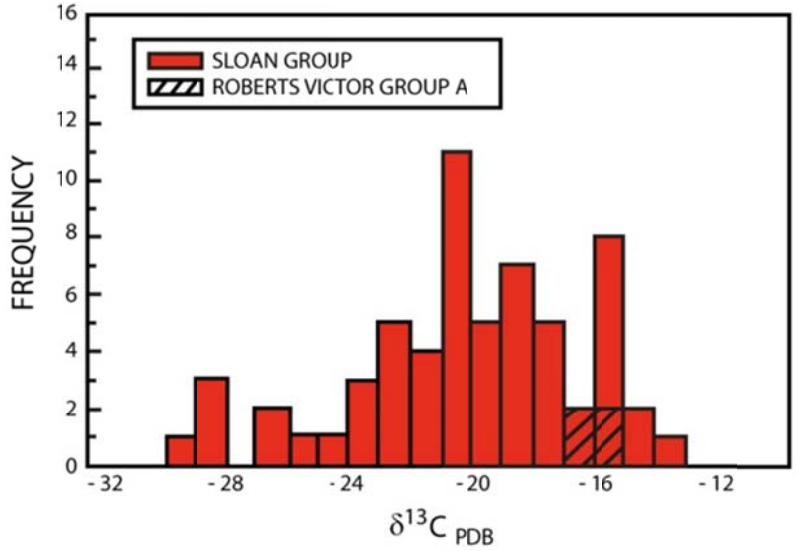

Figure 5. Histogram comparing the isotopic composition of the diamonds from the Sloan group (Sloan Ranch, Colorado) with those from the Roberts Victor group (Melissa et al., 1995)

Carbon isotopes are used to identify the origin of diamonds. The histogram in figure 5 is used to illustrate the range of organic carbon. Organic carbon is carried into the mantle along subduction zones, while inorganic carbon is thought to come from the mantle itself. Diamonds formed by organic carbon usually show an inhomogeneous isotope pattern (Fig 5), whereas diamonds formed by inorganic carbon will show a homogeneous isotope pattern (Melissa et al., 1995)

^{13}C values of 2 to -10 are indicative of inorganic carbon, whereas values of -12 to -30 are suggestive of organic carbon (Fig.5). A ^{13}C isotopic value of -16 is thus typical for diamonds formed by organic carbon. This is seen in the eclogitic diamonds from the Roberts Victor mine (Fig.5).

2.3 Previous Studies of Micro Diamonds

Micro diamonds as well as larger diamonds are known to be formed at high pressure and temperature conditions in the diamond window by polymorphic phase transformation of graphite into diamond (Fig.4). The temperature and pressure condition where this transformation takes place is at about 1000 to 1100°C and 45 to 50 kbar. Micro diamonds can also be formed due to shock metamorphism in the gas phase as seen in the Nördlinger Ries, Germany (Posges, 2005). Experimental studies on the formation of micro diamonds indicate that these types of diamonds can also be formed at medium to low pressure conditions. This process may even occur close to the Earth´s surface by the transformation of carbon-containing molecules into diamond (Rudenko et al., 1993; Rudenko and Kulakova., 1996).

These authors developed a model of non-equilibrium growth of diamonds in a macroscopic open catalytic system. All known active catalysts can be found in a kimberlite. Kimberlites originate from deep fractures in the Earth´s mantle. A Kimberlite retains a large number of gas channels and these different gases are involved in allochemical reactions which take place inside the pipe. Physically spoken, the most advantageous range of micro diamond formation is defined by a certain atomic ratio of C:O:H atoms in the original gas phase or plasma and the according temperature (Bachmann et al., 1991).

From a chemical point of view, the synthesis of micro diamonds and other carbon substances have different types of carbon-carbon bonds and as a result form polycarbons. These polycarbons are products of different chemical reactions (Rudenko and Kulakova., 1993). Polycarbons like diamonds, graphite and carbon are condensation products, created in a polycondensation process. If polycondensation under favourable conditions takes place, diamonds can be formed in the gas/plasma phase at low to medium pressure conditions according to the following reactions (Rudenko and Kulakova., 1996).

$2CO = C_{Di} + O_2$ (a)

$CO + H_2 = C_{Di} + H_2O$ (b)

$CH_4 + CO_2 = 2C_{Di} + H_2O$ (c)

$CH_2O = C_{Di} + H_2O$ (d)

$CH_3OH = C_{Di} + H_2 + H_2O$ (e)

$CH_4 = C_{Di} + 2H_2$ (f)

The polycondensation process is governed by two critical factors: First, the formation of a critical diamond nucleus and secondly the formation of the diamond crystal itself. An open catalytic system not in equilibrium is required to form diamonds in the gas/plasma phase and can be described by following equations:

$K + nA = \{A_n\}K \rightarrow \{A_n - mL\}K + mL$ (g)

A represent a carbon-bearing molecule, which is a polymeric monomer, $\{A_n\}K$ is a polymeric condensation product, which became absorbed by the catalytic converter, ***n*** is the number of molecular condensation, $\{A_n - mL\}K$ are the solid condensation products, which are diamond crystals and **L** describes light molecules such as H_2O and CO_2, which are removed during polycondensation (Rudenko and Kulakova., 1996).

$$A \rightarrow \left\{ \frac{nA \leftrightarrow C_{Di} + mL}{K \sum_i (C_{Di})_i} \right\} \rightarrow L \qquad \text{(h)}$$

The permanent addition of light carbon bearing molecules **A** and the subsequent subtraction of light molecules **L** (H_2O, CO_2) leads to disequilibrium in the open catalytic system described in equation ((g) and (h)). Kimberlites can act as a macroscopic open catalytic system and can thus be described by equation (h) to form diamonds under favourable kinetic and thermodynamic conditions according to the reactions (a) – (f) (Rudenko and Kulakova., 1993).

If equilibrium condition in the system (h) is reached, meaning **A = L** or the whole system becomes stagnant, then the formation of diamonds will stop immediately. Due to permanent formation of serpentine and carbonate bearing minerals the C:O:H ratio will change continuously and therefore disequilibrium can be expected until the emplacement of the kimberlite close to the Earth´s surface. Carbonate and serpentine forming reactions in the

kimberlitic melt therefore has a strong influence on the C:O:H ratio in the gas/plasma phase. Allochemical reactions will take place as a result of the accumulation of H_2O and CO_2 with the surrounding material. Carbonate and serpentine reactions act as a catalytic converter causing the formation of micro diamonds in serpentine and carbonate bearing veins. These veins crosscut the mantle xenoliths (Rudenko et al., 1993; Rudenko and Kulakova., 1996).

Chapter 3: Petrography

3.1 Sampling

The eclogitic samples collected from the Roberts Victor diamond mine, South Africa measured 40 cm x 20 cm x 10 cm (Fig. 6) and were ellipsoidal in shape. The chosen samples had metasomatised rims and contained garnets and omphacites that are the main rock forming-minerals in eclogites.

Figure 6. Disc shaped eclogite from the Roberts Victor mine, South Africa

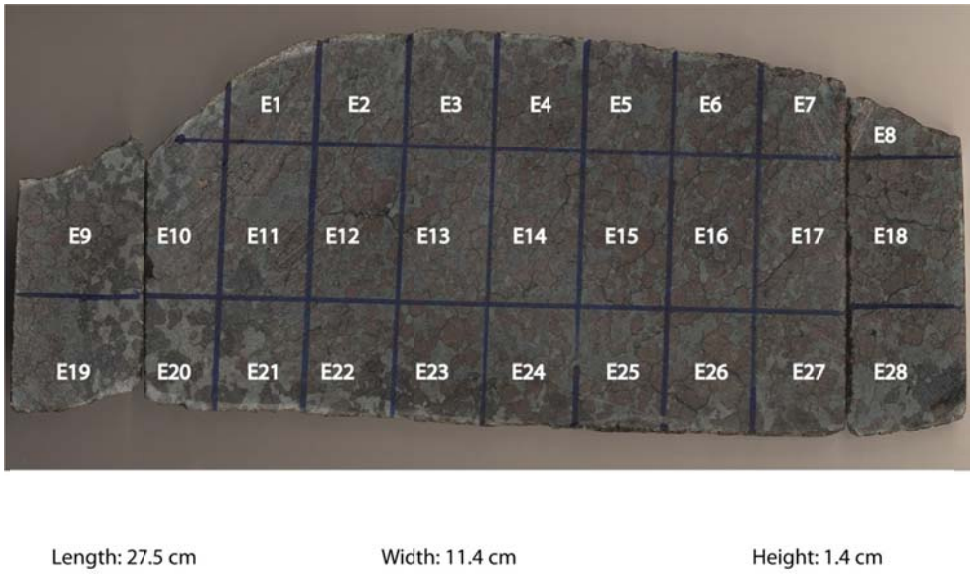

Figure 7. Eclogite slice showing the areas selected for thin sections

The samples were then cut into slices (Fig. 7). These slices were further cut into 28 thin sections (Fig. 8) from which four were selected for detailed analysed for this thesis. The minerals can clearly be seen in the thin sections. These minerals include brownish garnets, green omphacites and dark coloured serpentine veins. The serpentine veins also contain white carbonate minerals.

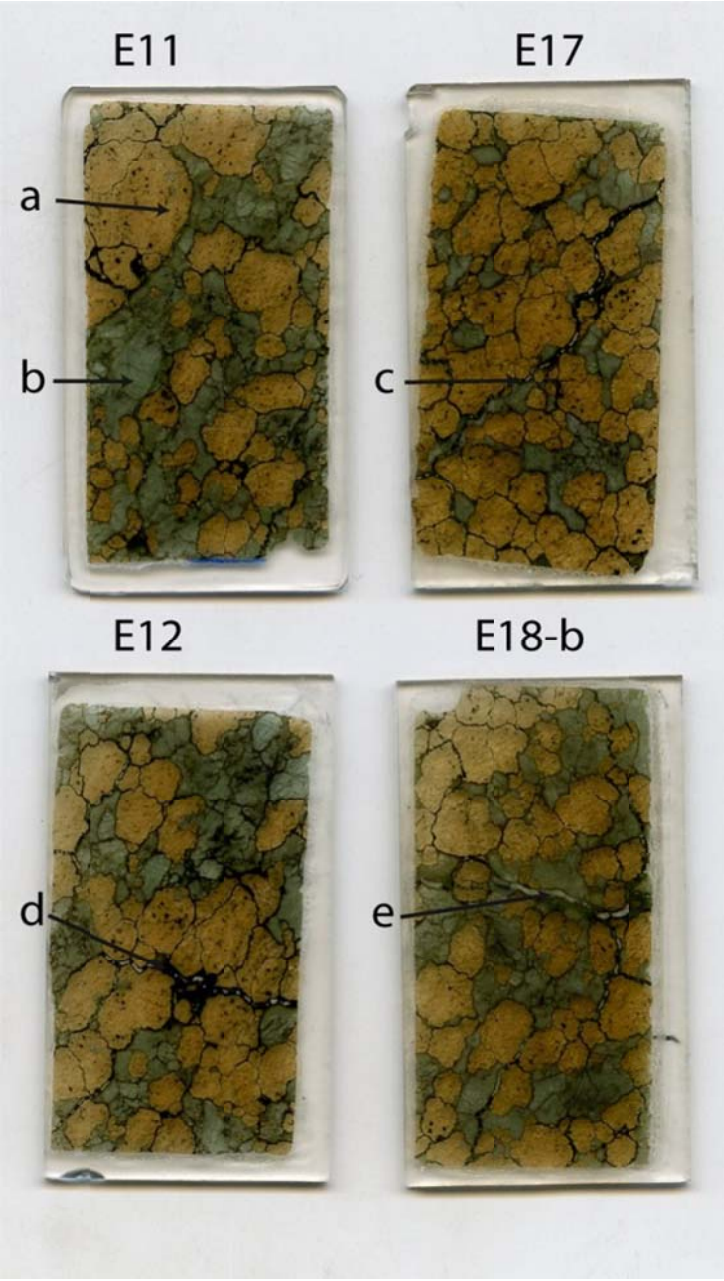

Figure 8. Thin sections made from the eclogite sample. a: garnet crystal, b: omphacite crystal, c: serpentine vein, d: carbonate crystals within the serpentine vein and e: carbonate-bearing vein.

3.2 Indicator Minerals

Indicator minerals are minerals, which due to weathering processes get washed out of the kimberlites/lamproites. These minerals such as garnet are unaffected by alteration processes and can be found in sediments. They have a distinguishing mineral chemical composition, which can be used as a diamond tracer in kimberlites/lamproites.

A Mineral that is an ideal indicator is a garnet with a high XMg ratio as well as a high Cr and a low Ca concentration ("G10-Grt"). Ca-rich garnet-lherzolites ("G9-Grt") cannot be used as indicators for diamonds. High Mg and Cr concentrations in chromites can also be used as a diamond indicator. E-type diamonds are always associated with Na- and Ti- rich garnets (melanite component) (Gurney et al., 1993).

It is for this reason that garnets were used in this study.

3.3 Macroscopic Rock Description

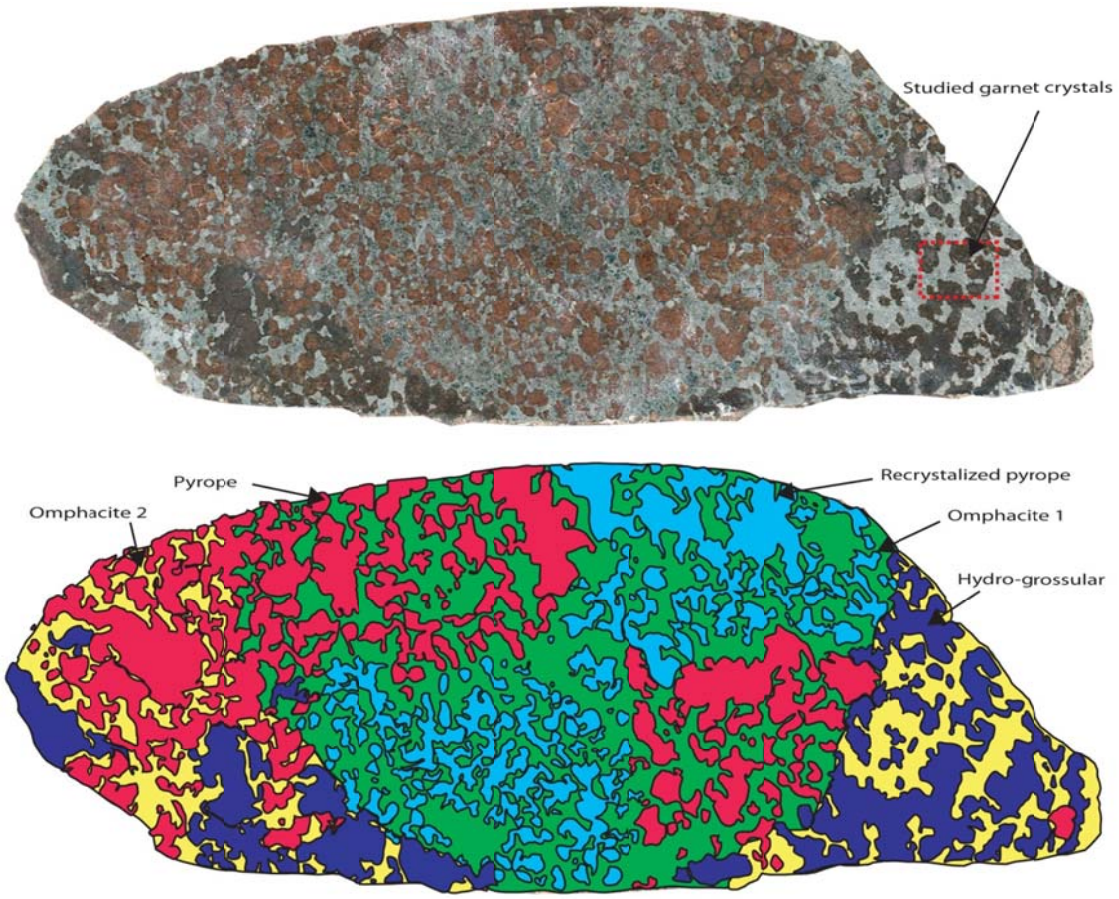

Figure 9. Eclogite from the Roberts Victor mine showing metasomatised rims (Potgieter, 2009).

The studied eclogite shows a wide variation in mineral chemistry. The garnets found in the sample vary from magnesium-rich Pyropes (red) in the center to more hydro-grossular-rich garnets (dark blue) at the rims (Fig 9). The clinopyroxenes also vary from sodium-rich jadeite (green) in the center to calcium-rich diopside (yellow) at the rims of the sample (Fig. 9). Both clinopyroxenes are of omphacitic composition. Recrystallized pyrope (light blue) is found in the center of the studied sample.

3.4 Microscopic Description

3.4.1 Minerals

3.4.1.1 Garnet $(Fe, Mg)_3Al_2Si_3O_{12}$

The garnets (Grt) seen in the studied eclogite sample are pale brown to reddish in thin section. They are isotropic and have a high refractive index. The crystals are euhedral to subhedral and contain micro cracks (Fig. 10). Some of these micro cracks may contain micro diamonds. Pyroxene inclusions have also been observed in the garnet crystals. The garnets show no signs of alteration. The garnets are often surrounded by late forming serpentine (Serp) veins (Fig. 11).

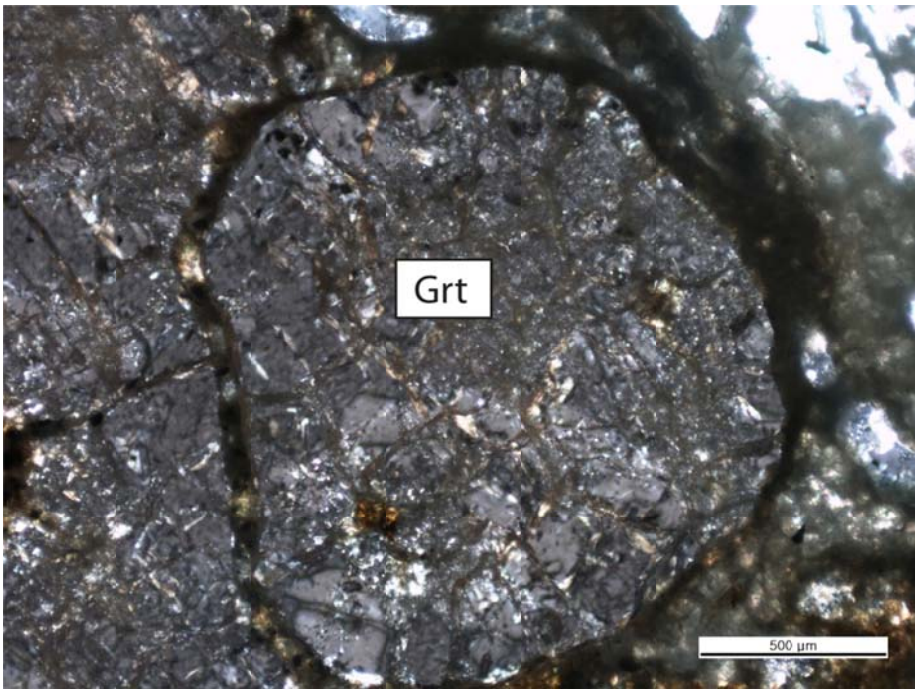

Figure 10. Inhomogeneous garnet crystal under crossed nicols using transmitted light surrounded by a serpentine vein.

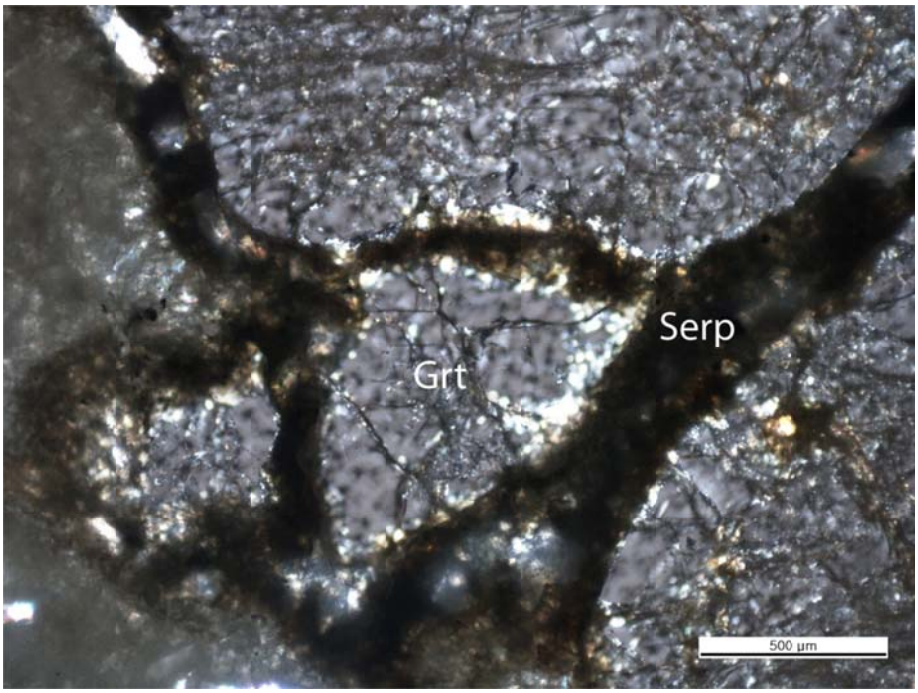

Figure 11. Garnet crystals surrounded by late forming serpentine veins. As seen under crossed nicols in transmitted light

3.4.1.2 Omphacite (Na, Ca)(Mg, Fe, Al) Si_2O_6

The omphacite (Omph) in this sample appears pale green to colourless in thin section. The shape of the crystals is anhedral. A distinctive 90° cleavage can easily be seen in some of the crystals. Second order interference colours can be seen in thin sections (Fig. 12). The omphacites observed in this sample also exhibited irregular cracks. Fig. 13 shows that the omphacite crystals may also be surrounded by serpentine veins.

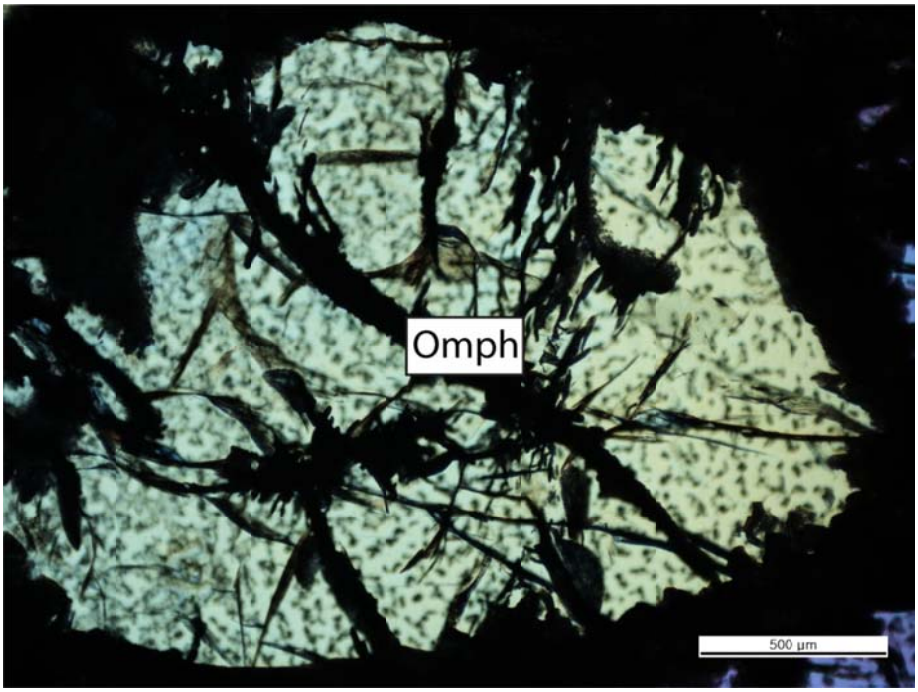

Figure 12. Omphacite crystal under crossed nicols in transmitted light showing 90° cleavage. Irregular cracks can also be seen in this figure

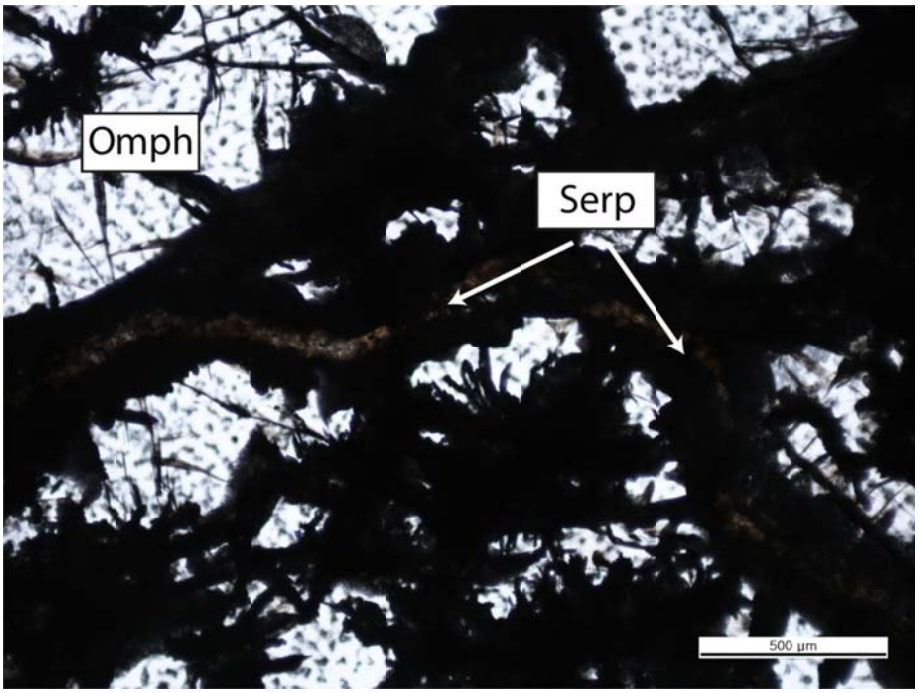

Figure 13. Omphacite crystals surrounded by late formed serpentine veins under transmitted light

3.4.2 Accessory Minerals

3.4.2.1 Serpentine $(Mg, Fe)_3Si_2O_5(OH)_4$

The serpentine (Serp) crystals seen in this sample are massive in habit. These minerals appear brown to black in thin section (Fig. 14). They are also veined. Some are intergrown with other minerals such as calcite (Cal).

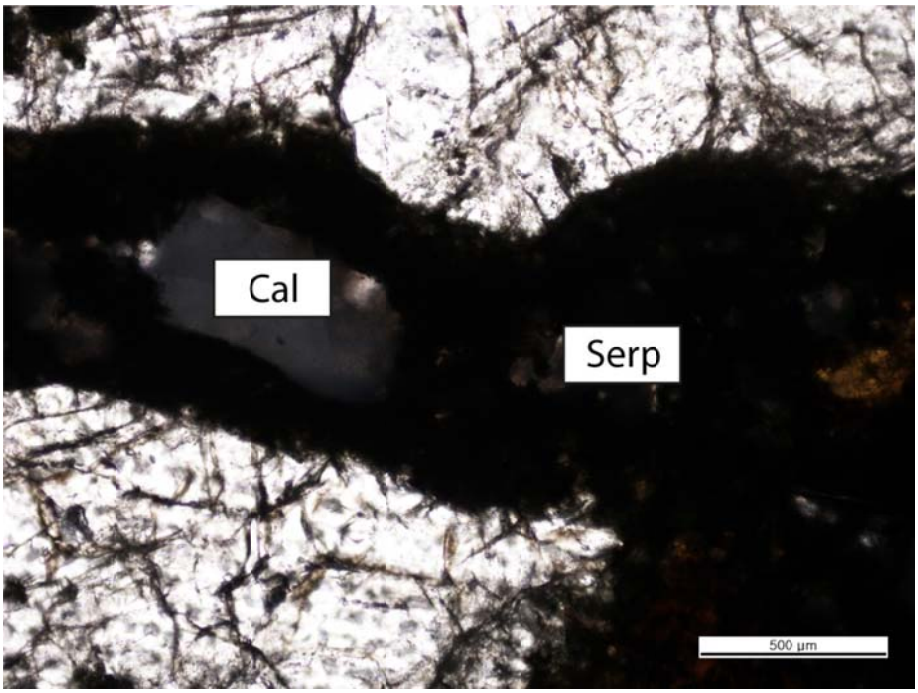

Figure 14. Serpentine vein with calcite inclusion as seen in transmitted light

3.4.2.2 Biotite K(Mg, Fe)3AlSi3O10(F, OH)2

Minor amounts of biotites where found in the studied sample. This mineral appears brownish in the studied thin sections and also exhibits perfect basal cleavage. Biotite forms pseudohexagonal crystals. It can also be identified by the gnarled bird's eye extinction under crossed polarised light.

3.4.2.3 Amphibole

Amphibole occurs as an accessory mineral in the studied sample. This mineral is dark in color. No further studies where done on amphibole.

3.4.2.4 Diamond (C)

The diamonds found in the studied eclogite sample are small (50 to 1µm) in diameter. These diamonds occur within three different settings in the collected samples. Diamonds are found within the garnet and omphacite crystals (Fig. 20), in the serpentine veins (Figs. 15, 16, 17, 18, 19 and 28) as well as in the micro cracks (Figs. 21, 22, 23, 24, 25, 26, 27 and 29) found in individual garnet and omphacite crystals. The size of these diamond crystals vary depending on the setting. The diamonds found in the garnet and omphacite crystals are bigger than the diamonds that occur in the serpentine veins and within micro cracks in the garnet crystals. The shape of the diamonds that were observed within the micro cracks might be controlled by the width and/or length of the crack itself (Figs.21, 24, 25, 26, 27 and 29). The diamonds are usually well shaped and occur as bright white cubes under reflected light. All the back scatter electron pictures were taken with the SEM at the Seoul National University in South Korea.

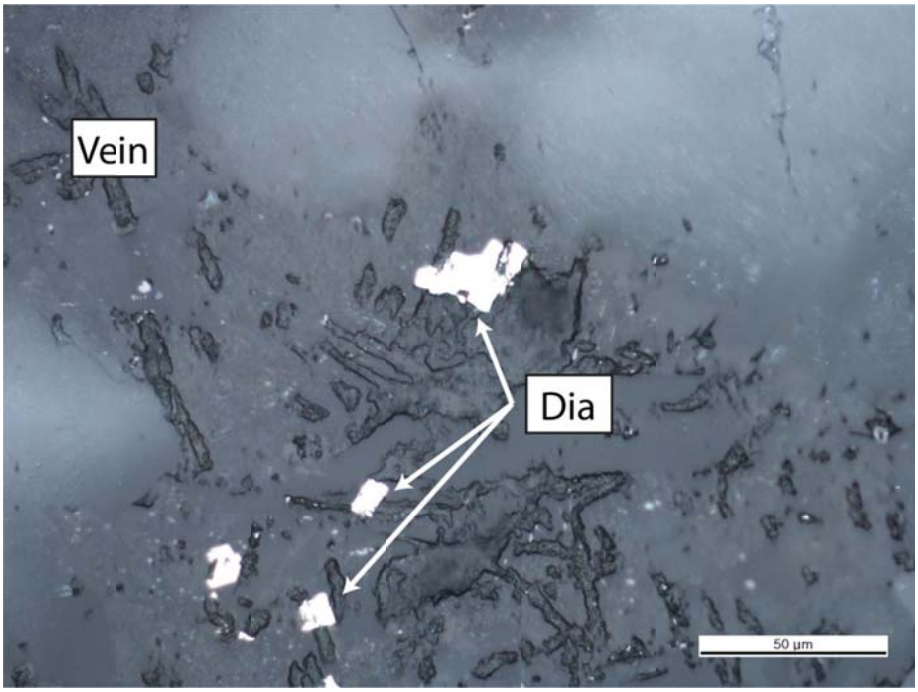

Figure 15. Micro diamonds in a serpentine vein as seen under reflected light

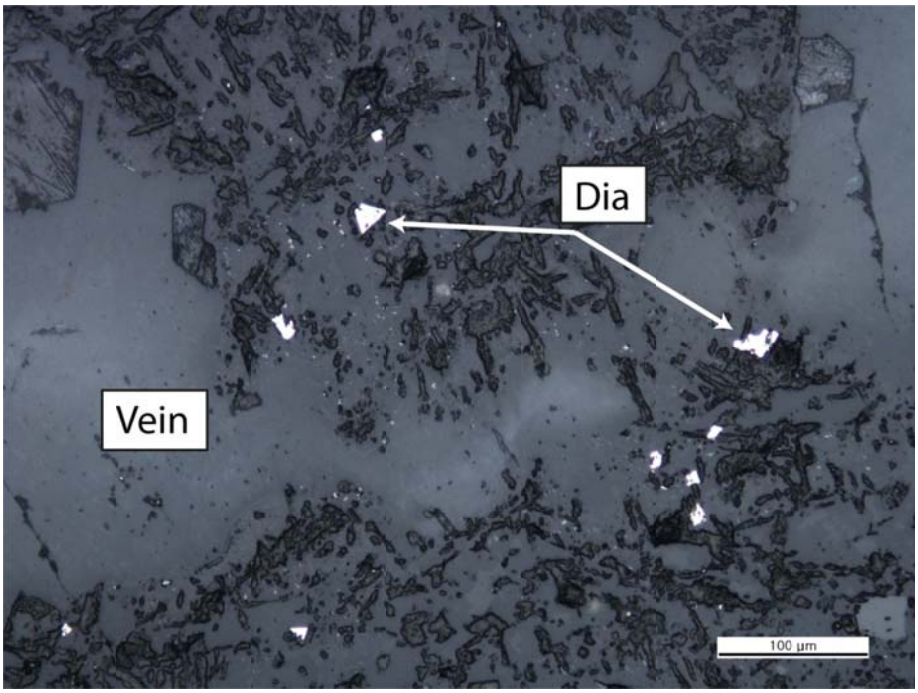

Figure 16. Micro diamonds in a serpentine vein. Reflected light was used

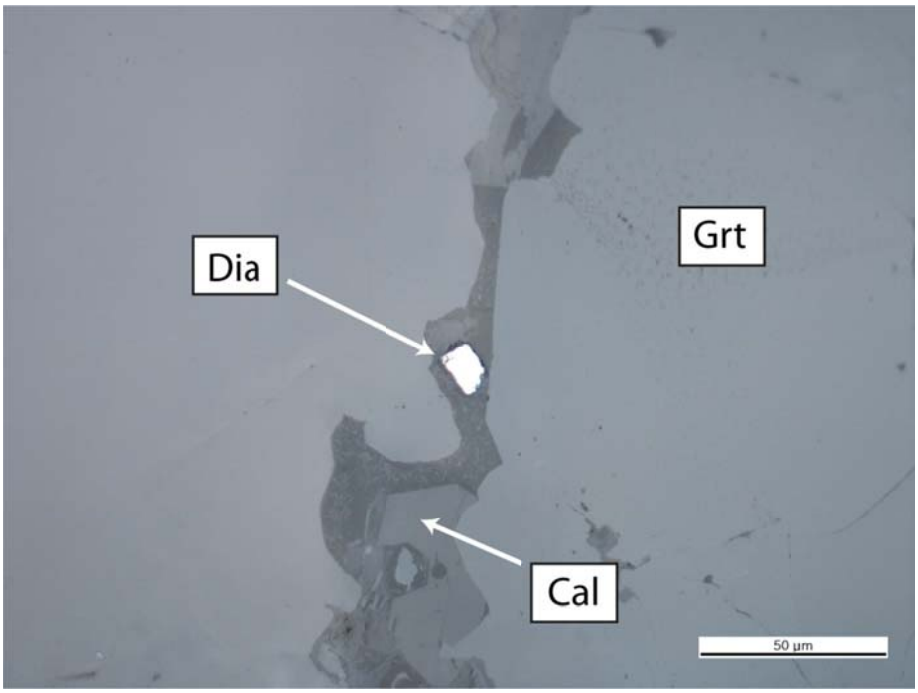

Figure 17. A cubic micro diamond in a serpentine vein in a garnet crystal. Calcite is also observed inside the serpentine vein. Reflected light was used

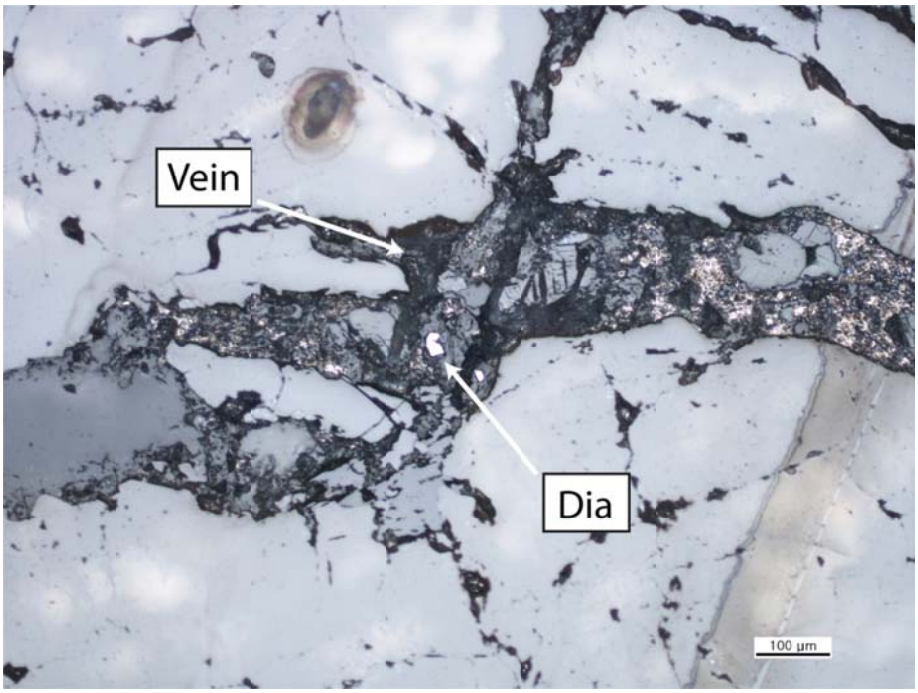

Figure 18. A serpentine vein inside a garnet crystal. Micro diamonds and calcite crystals can be observed inside the vein. Reflected light was used

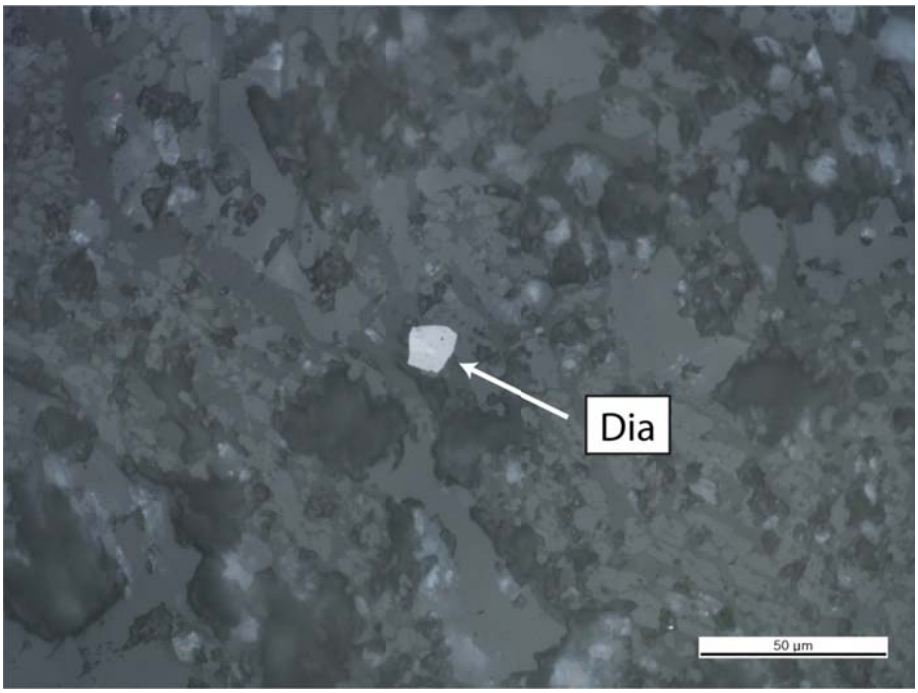

Figure 19. Micro diamond in a serpentine vein. Calcite is also observed. As seen under reflected light

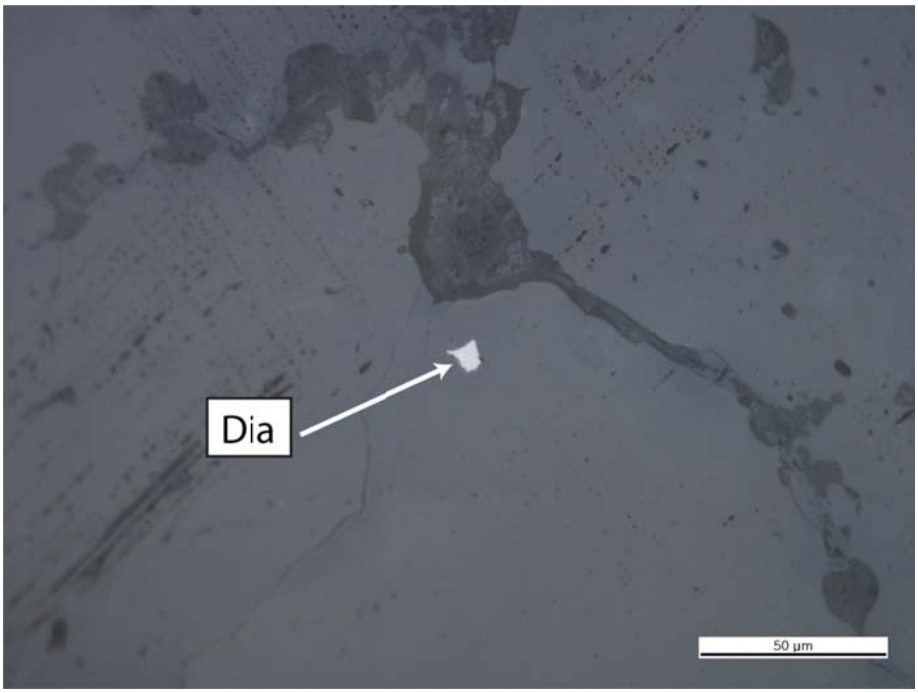

Figure 20. Micro diamond in a garnet crystal as seen under reflected light

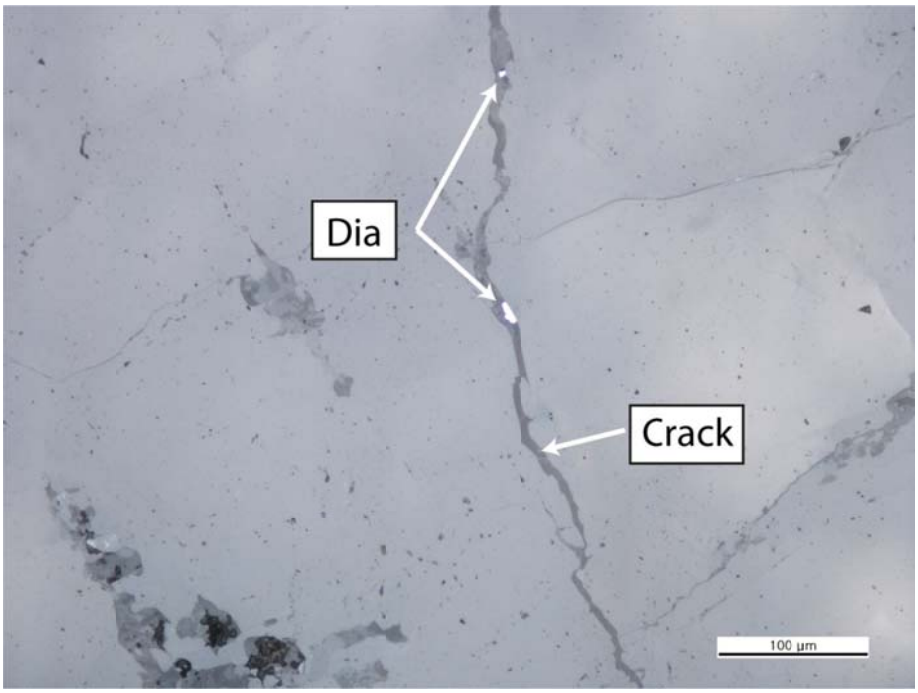

Figure 21. Micro diamonds in a crack in garnet. These diamonds are 1 µm in diameter. Reflected light was used

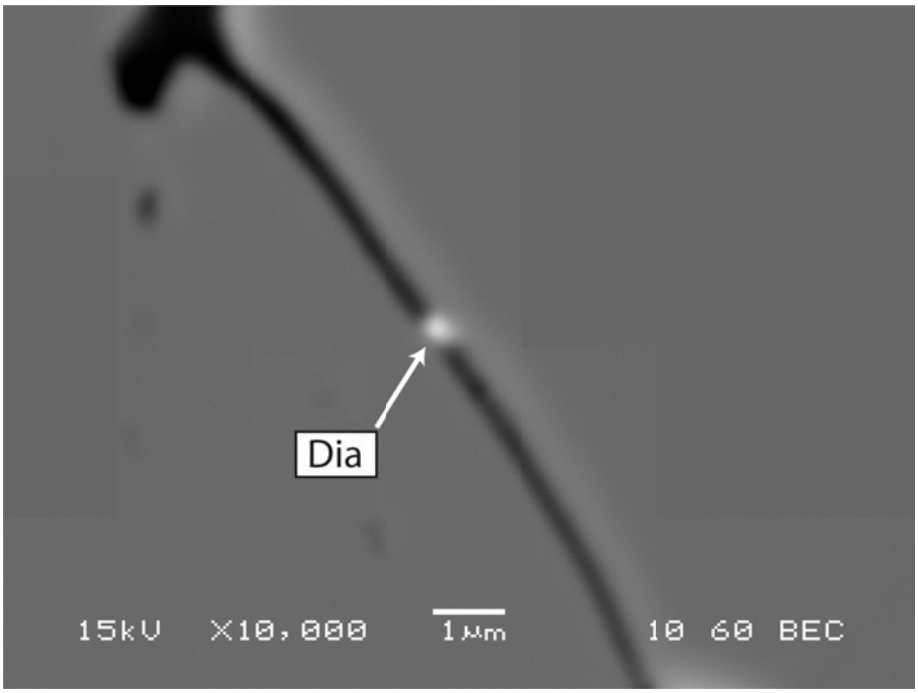

Figure 22. Back scatter electron (BSE) image of a micro diamond in a crack inside a garnet crystal

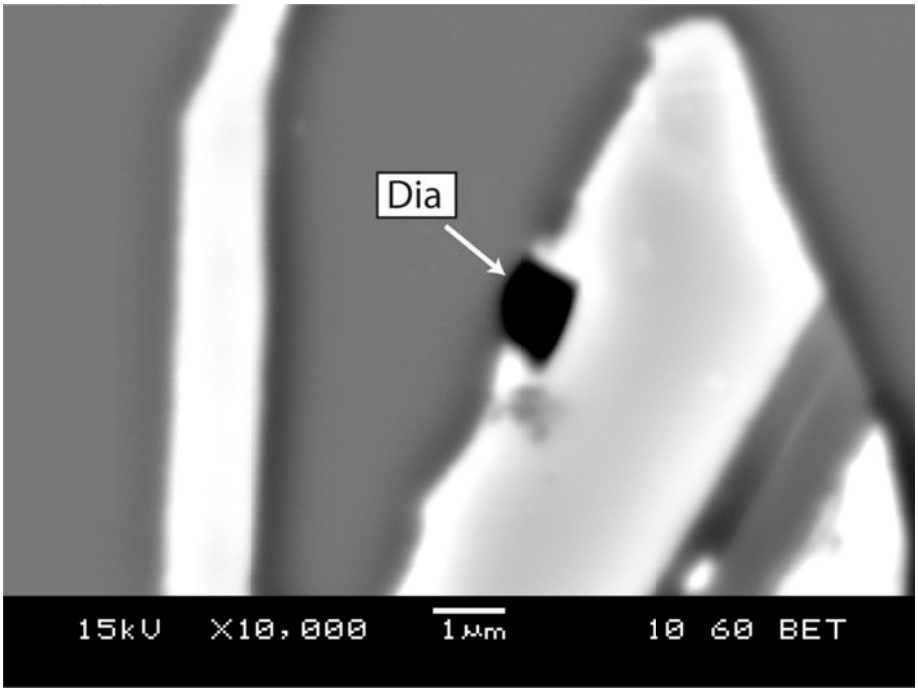

Figure 23. A topographical BSE image of a micro diamond in a crack within a garnet crystal

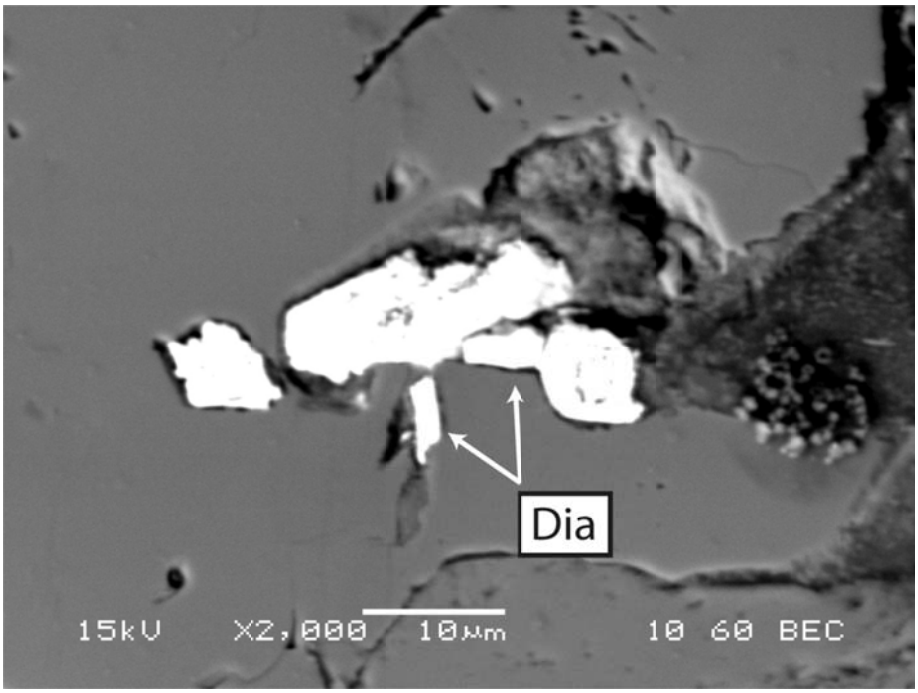

Figure 24. BSE image of micro diamonds in cracks located in a garnet crystal

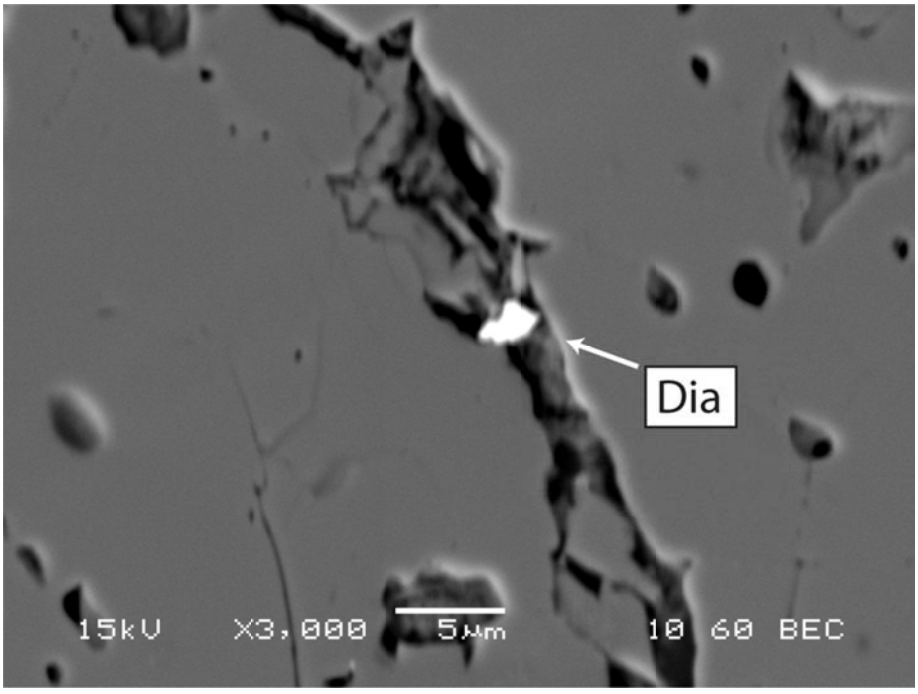

Figure 25.Micro diamond in a crack inside a garnet. SEM BSE image

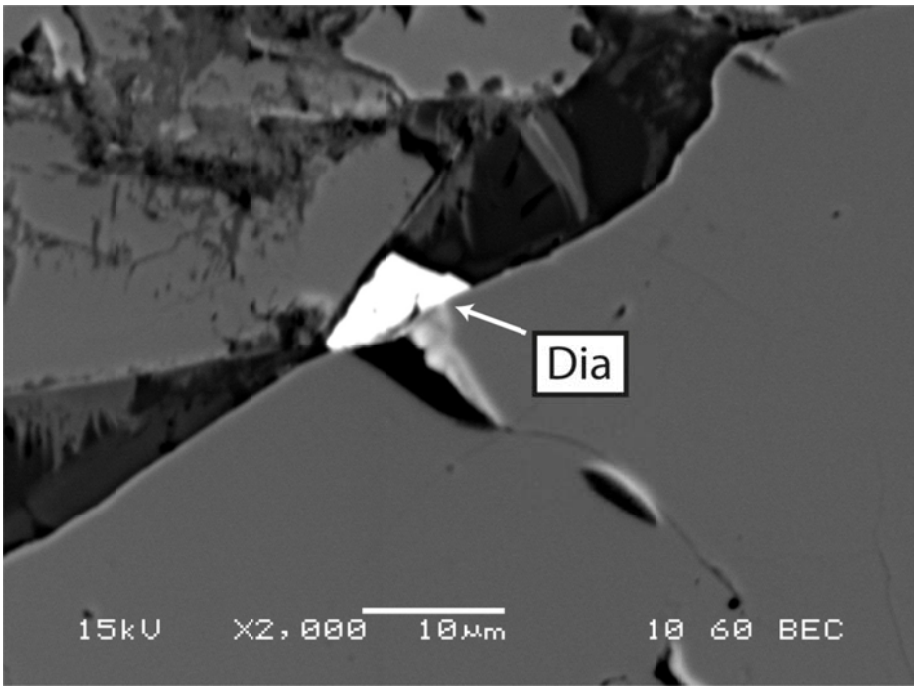

Figure 26. BSE image of a micro diamond in a crack hosted in garnet

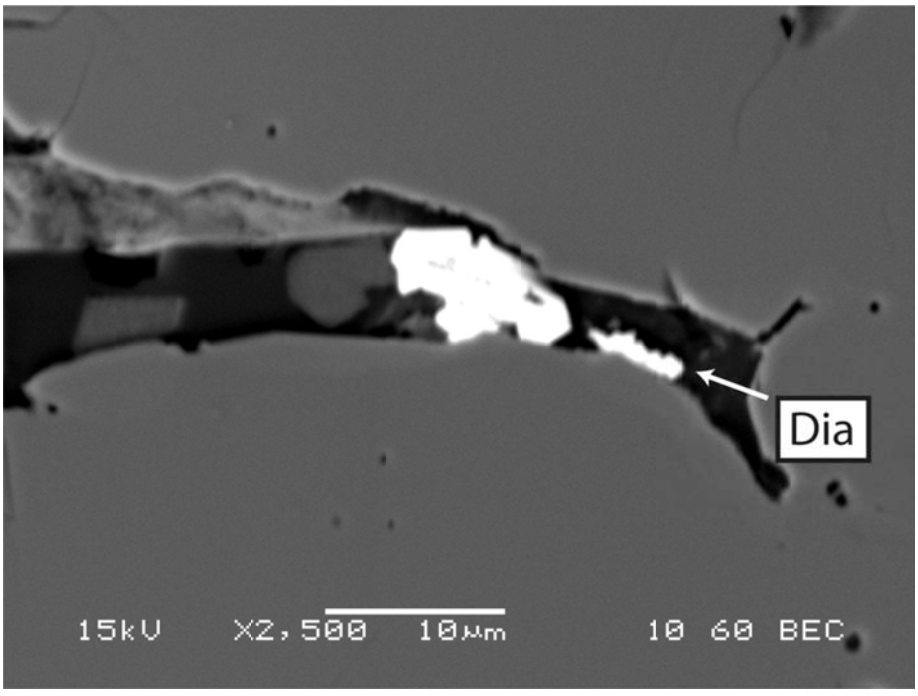

Figure 27. BSE image showing two micro diamonds in a crack in garnet

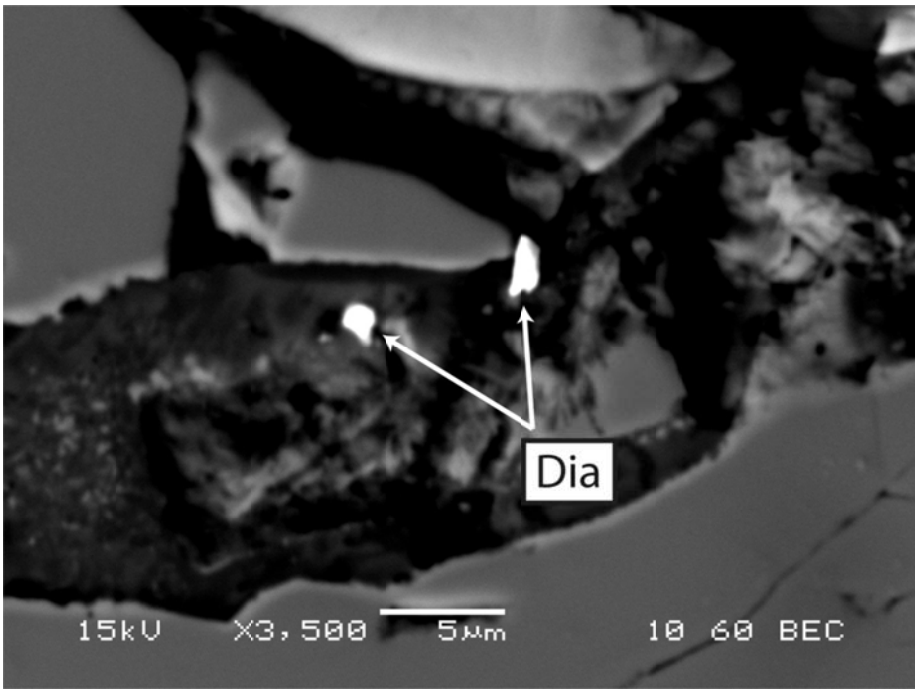

Figure 28. The BSE image shows two micro diamonds found in a serpentine vein

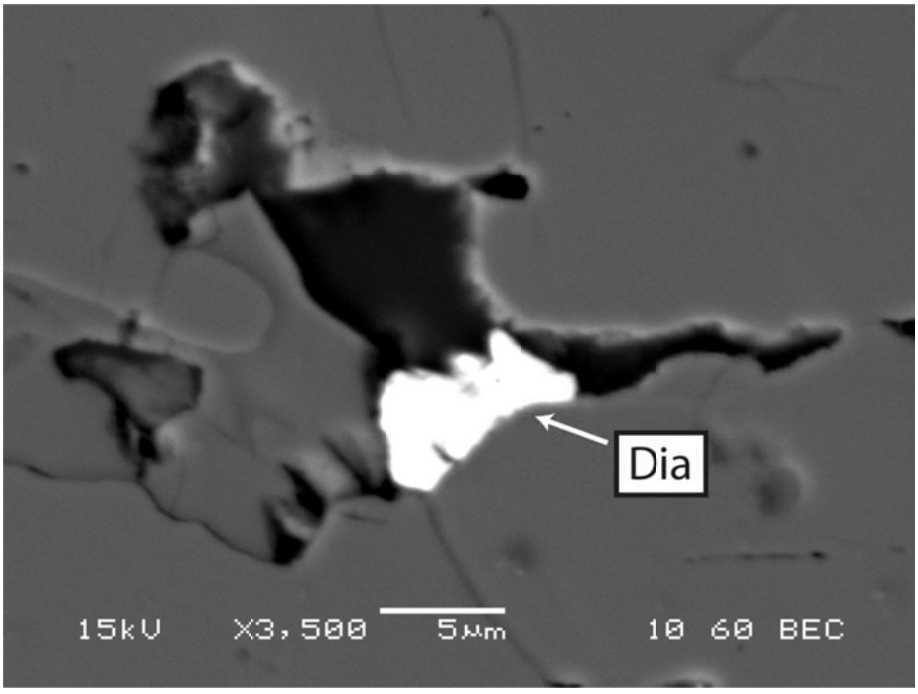

Figure 29. A micro diamond in a crack within a garnet crystal. The shape of the diamond appears to be controlled by the margins of the crack

Chapter 4: Micro Cracks

4.1 Definition of Defect Structures

Micro cracks are two dimensional defect structures. They can also be interpreted as mono mineralic grain boundaries. Three types of two dimensional defect structures occur: screw dislocation, edge dislocation and lineage structure (Fig. 30). The studied micro cracks within the garnet crystals are example of lineage structure defects. These lineage structures are characterized by high dislocations which facilitate volatile movement in the crystal matrix.

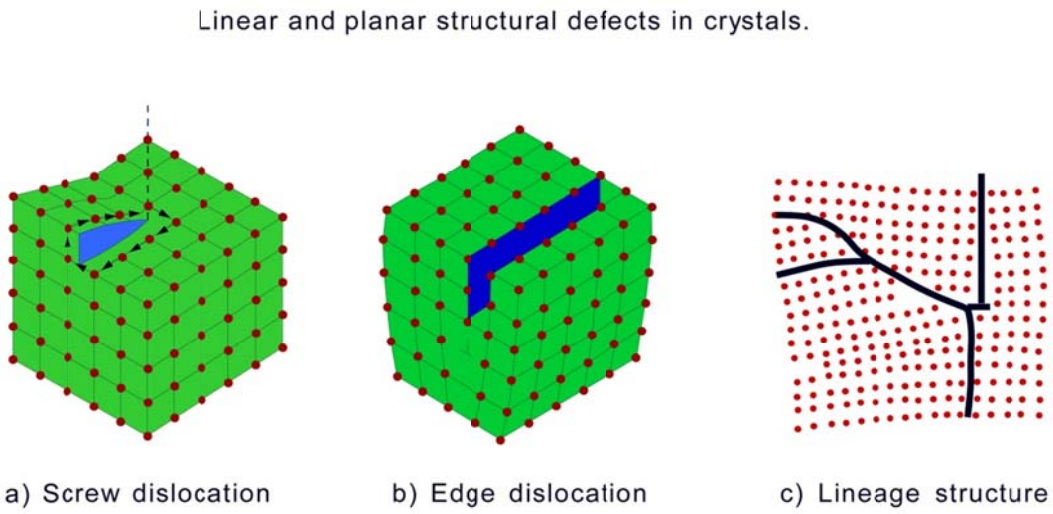

Figure 30. Defect structures in crystals (Bucher, 2002)

4.2 Micro Crack Description

The micro cracks in the studied eclogite are examples of lineage structures. They occur at the rims of the garnet and omphacite crystals. These micro cracks are not aligned and are found randomly in the studied minerals. In some cases they are interconnected to each other, but generally they occur isolated in the crystal matrix. These cracks are 0.1 to 0.3 μm wide and can be up to 100 μm long.

The micro cracks form between 50 and 60 kbar and at temperatures of ~ 1200°C. They act as pathways for fluid during uplift of the kimberlite and it is due to this fluid movement and chemical interaction that diamonds are formed in the cracks (Fig. 20). However not all the micro cracks contain micro diamonds, non-diamond bearing cracks are also widespread throughout the sample.

4.3 Formation of Micro Cracks

The formation of these micro cracks is due to decompression of the xenoliths, which takes place in the Earth´s upper mantle. Due to the fast ascent of the kimberlite through the Earth´s upper mantle and lithosphere, the density contrast between the kimberlitic melt and the xenoliths within in the kimberlitic melt changes continuously. The difference in density between the xenolith and the kimberlitic melt in the Earth's mantle is much higher than at the Earth´s surface. The density contrast at a depth at 150 to 160 km is in the order of magnitudes higher than at the Earth´s surface (Sommer et al 2009*b*).

The kimberlitic melt contains large quantities of volatiles. These volatiles mainly consist of H_2O and CO_2. Kimberlites are usually very CO_2 rich. This increase in CO_2 leads to an overall viscosity of less than 1 (the same viscosity as water). In general a kimberlitic melt has a viscosity of 0.5 (Sparks et al., 2006). When the kimberlite picks up the xenolith in the Earth´s upper mantle the kimberlitic melt has the consistency of a plasma or gas. As eruption of the kimberlite takes place, water and CO_2 is constantly being removed from the kimberlitic melt to form minerals such as serpentine and calcite. Consequently the density of the kimberlitic melt will change continuously, as a result of cooling. This is the reason for the decrease in density contrast between the kimberlitic melt, the country rocks and the xenoliths within the kimberlite during the uplift. The decompression cracks are thus formed in depth, where the highest density contrast occurs (Sommer et al., 2009b).

Chapter 5: Mineral Chemistry

5.1 Analytical Methods

28 thin sections of the studied eclogite were investigated using transmitted light microscopy and a scanning electron microscope (SEM). Four thin sections were then selected for detailed analyses. Mineral analyses were carried out in Graz using a JEOL 6310 SEM equipped with a LINK ISIS energy-dispersive system and a MICROSPEC wavelength dispersive system. Accelerating voltage was 15 kV and 5 nA. Matrix corrections for silicates were made using the ZAF procedure, and natural mineral standards were used for calibration. Detection limits varied 0.1 to 0.5 wt. % for the JEOL SEM with the LINK ISIS energy-dispersive system.

5.2 Minerals

5.2.1 Garnet

Core and rim measurements of the garnet crystals were taken in order to analyse the X_{Mg}, X_{Ca} and X_{Fe} variations present in the eclogite sample. An example of these measurements can be seen in figure 31.

The formula used for these measurements is: $X_{Mg} = \frac{Mg}{Mg+Fe+Ca}$

$$: X_{Fe} = \frac{Fe}{Mg+Fe+Ca}$$

$$: X_{Ca} = \frac{Ca}{Mg+Fe+Ca}$$

The X_{Mg} varies from 0.596 at the rim to 0.550 units per formula at the centre of the sample. These measurements thus show that the X_{Mg} is higher at the rims of the garnet sample than in the middle.

The X_{Fe} varies from 0.322 units per formula in the centre of the garnet crystal to 0.259 units per formula at the rim of the sample. This is in contrast to the X_{Mg} measurements due to the FM exchange.

The X_{Ca} varies from 0.150 units per formula in the centre to 0.127 units per formula at the rim of the studied garnet sample. These results thus indicate that the X_{Ca} is higher at the centre of the garnet crystal than at the rims.

Refer to the appendix for the micro probe analyses.

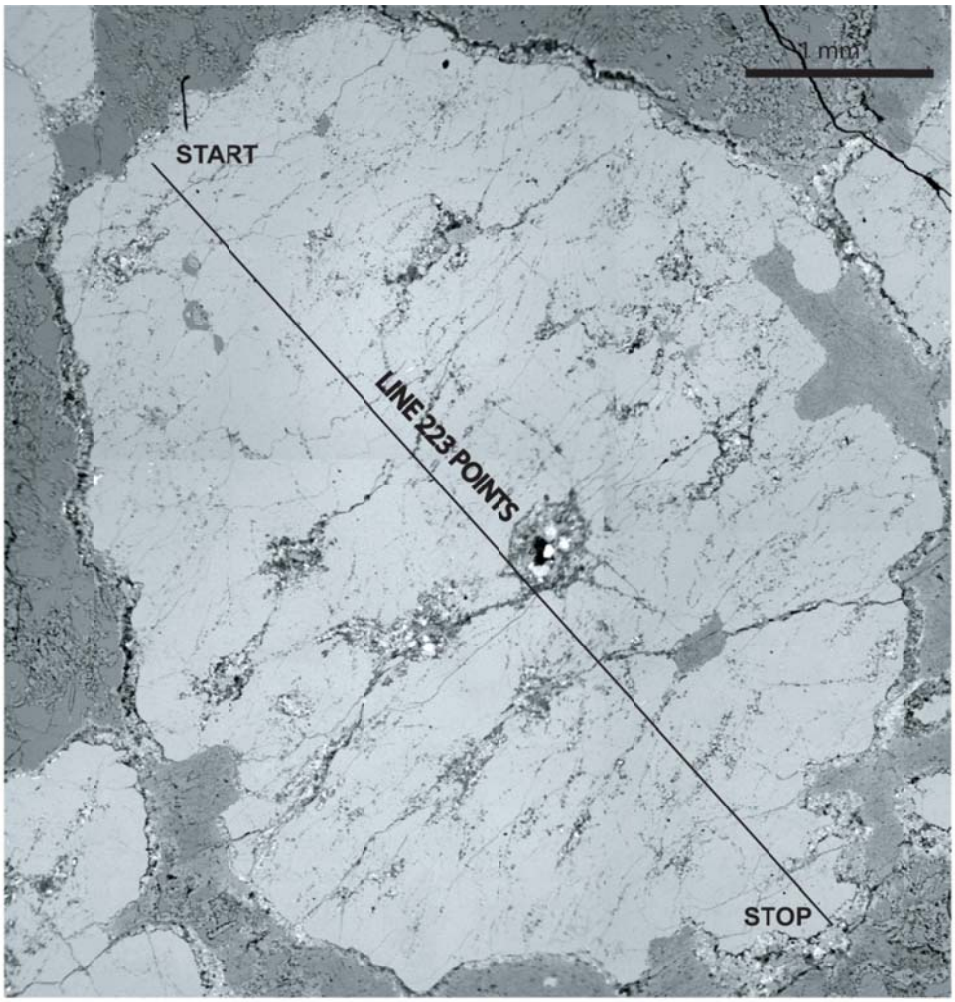

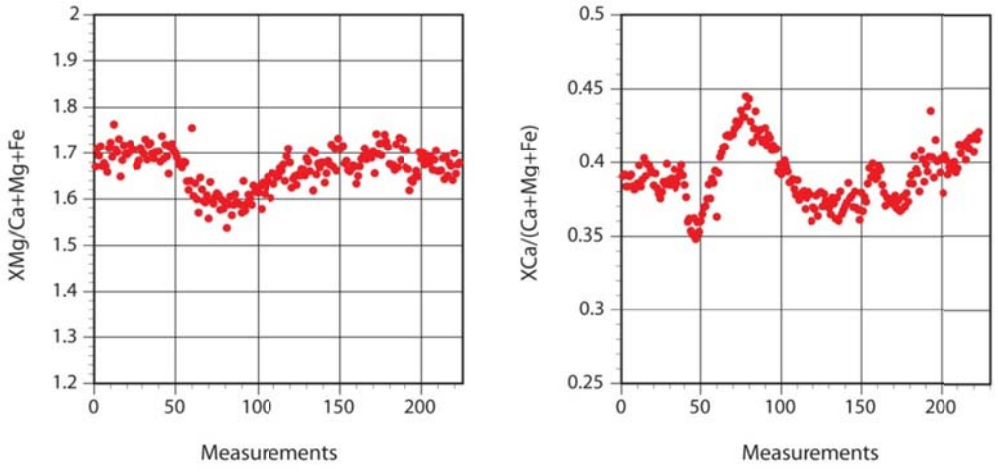

Figure 31. Garnet crystal showing the X_{Mg} and X_{Ca} ratios. Measured with SEM with EDX and WDX. The garnet crystal measures 5mm and 223 points were analysed

5.2.2 Omphacite

Core and rim measurements of the omphacites where analysed. These measurements showed that the studied omphacites were homogeneous and showed no chemical zonation as is the case in the garnet samples. The X_{Mg} of the studied mineral samples are homogeneous in nature and varies between 0.79 and 0.82 atomic units per formula. A strong dissimilarity is visible in the X_{Al}, X_{Ca} and X_{Na} concentrations measured. X_{Al} varies between 0.09 to 0.25 atomic units per formula, X_{Na} between 0.05 and 0.31 units per formula and X_{Ca} between 0.58 and 0.75 units per formula (refer to appendix).

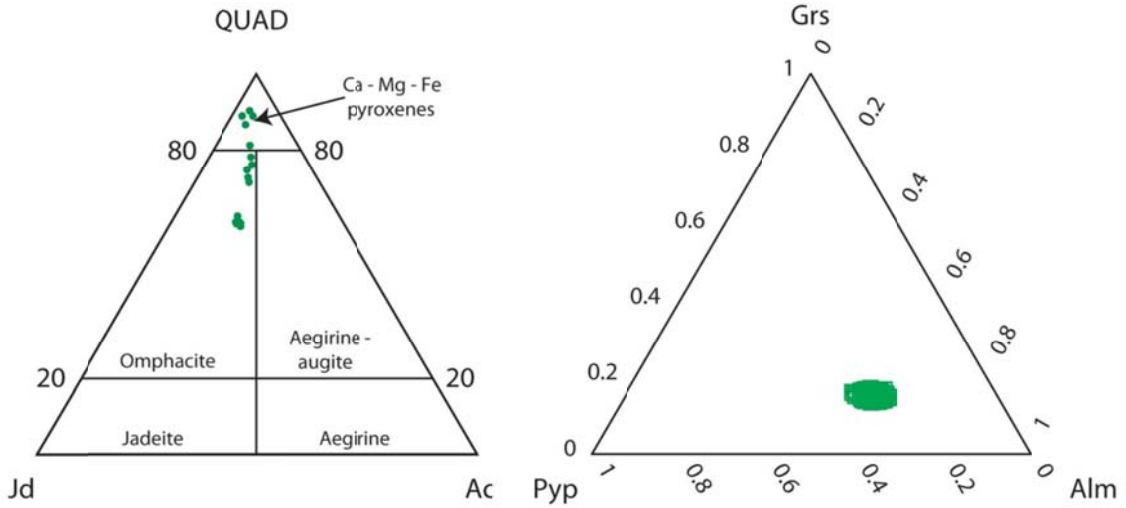

Figure 32. Plots for pyroxenes and garnets. The pyroxene plot indicated that the studied sample contains diopsides as well as omphacites. The garnets located in the eclogite sample have an almandine/pyrope composition

The pyroxenes found in the rims of the eclogite sample (Fig.9) are Ca-rich whereas the pyroxenes located in the centre of the sample are more Al and Na-rich. This indicated that the pyroxenes located in the rims of the sample are diopsides while the pyroxenes found in the centre of the sample have an omphacitic composition (Fig. 32). The following reaction thus took place in the sample: 2Ca = Al + Na.

5.3 Accessory Minerals

5.3.1 Biotite

The biotites located in the eclogite sample have an X_{Mg} between 0.76 and 0.79 units per formula which is indicative for phlogopites. Refer to the appendix for the micro probe analyses.

5.4 Conclusion

The results of the core to rim measurements of the garnets in the eclogite sample (Fig.31) showed that the changes in the X_{Mg} and X_{Fe} ratios may be due to the sample undergoing metasomatism and thus being heated from the rims to the centre during uplift. The change in the X_{Ca} ratios from the core to the rim of the measured garnet crystals of the eclogite sample demonstrates that the sample was formed at high pressure conditions. Since the measurements decrease from the centre to the rim it can be deduced that the pressure dropped while the eclogitic xenolith was brought to the surface of the earth by the kimberlite (Deer et al., 1992).

It was discovered that the studied eclogite sample contained diopside as well as omphacite. The omphacite crystals were analysed and strong variations in the X_{Ca}, X_{Na} and X_{Al} ratios were discovered. These variations are thought to be due to decompression (decrease in pressure) caused by the uplift of the eclogite xenolith. The diopsides discovered in the rims of the studied eclogite (Fig.9) sample are indicative of high temperature conditions and the omphacites found in the centre of the sample shows that the eclogite was formed under high pressure conditions (Deer et al., 1992).

Chapter 6: Micro Diamonds

6.1 Introduction

The high-pressure modification of carbon is known as a diamond. When a diamond is well crystallized, they occur as octahedrons, but cubes and cube-octahedral forms are also common, whereas rhombododecahedrons are very rare. Cubes and cube-octahedrons are formed at higher pressures and lower temperatures. Diamonds from eclogites and peridotites from the same deposit are formed under similar conditions. Typical depth ranges between 150 and 200 km and temperatures below 1200 °C. Some E-type diamonds are formed at depth of about 400 km (Spear., 1993).

The micro diamonds found in the studied eclogite sample can be divided into three groups. They are micro diamonds found in the garnet and omphacite crystals itself, micro diamonds in the micro cracks within the garnet crystals and micro diamonds in the serpentine veins.

The micro diamonds found within in the garnet and omphacite crystals are usually larger than the other types of diamonds found in the sample. This is due to the fact that they were formed at greater depths and temperatures in the mantle. They thus had more time to form bigger diamonds. These micro diamonds are also well shaped. It is thought that the micro diamonds found in the micro cracks within the garnet crystals were formed at shallower depths and cooler temperatures, thus forming smaller crystals. The serpentine veins contain the most micro diamonds. These diamonds are larger than those found in the micro cracks. They are also better shaped.

6.2 Analytical Methods

Diamonds were identified by using a dispersive DXR Raman spectroscopy (Thermo Scientific) at the Tectonophysics Laboratory of the School of Earth and Environmental Sciences (SEES), Seoul National University.

The Raman microscope was equipped with a 532-nm laser, a standard resolution grating (5 cm^{-1} nominal resolution, 50-3550 cm^{-1} spectral range), and an optical microscope (Olympus, 50x objective). The Raman spectrum was obtained from 30 μm beneath the surface and around the embedded crack. An exposure time of 22 seconds and a laser power of 10 mW was used.

6.3 Micro Diamond Types

According to a study done by Rudenko et al., 1993 (see Chapter 2.3), micro diamonds can be formed at medium to low pressure conditions in serpentine veins and in two dimensional defect structures such as micro cracks. Different chemical reactions may lead to the formation of differently shaped micro diamonds. It is also thought that the chemical reactions will differ depending on the location inside the studied eclogite sample (Fig.6) for example within the garnet or omphacite crystals (Fig.20), the serpentine vein (Fig.18) or the micro crack within a garnet crystal (Fig.27). Micro Raman analysis was thus done in order to determine if shifts can be observed in the Raman spectra from these three different locations.

6.3.1 Micro Diamonds within Garnet and Omphacite Crystals

These micro diamonds are found within garnet and omphacite crystals in the studied eclogite sample. The Raman peaks observed between 350 cm^{-1} and 390 cm^{-1} are indicative of the garnet matrix/crystal hosting the micro diamonds. Two peaks that are suggestive of the micro diamonds were found in the samples analysed. One peak was found at about 1322 cm^{-1} to 1325$cm^{-}1$, while another diamond peak was observed at about 1331 cm^{-1} to 1336 cm^{-1}. In some cases both peaks were observed in the same samples as can be seen in figure 34 where diamond peaks were observed at 1331.98 cm^{-1} and 1322.67 cm^{-1}. In most cases however only one micro diamond peak can be seen (fig. 33, 35, 36 and 37).

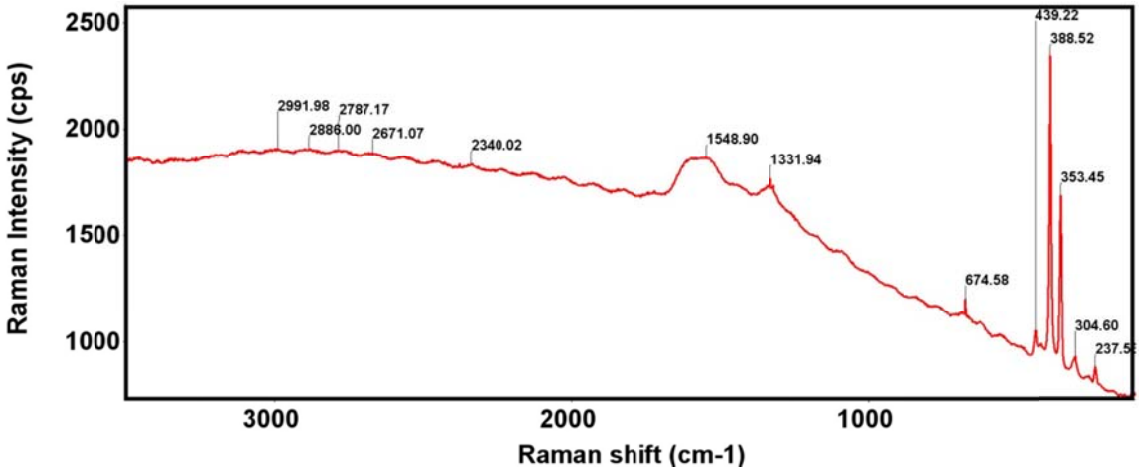

Figure 33. A diamond peak can be observed at 1331.94 cm^{-1}. The peaks ranging between 353.45 cm^{-1} and 388.52 cm^{-1} are indicative for the garnet matrix/crystal

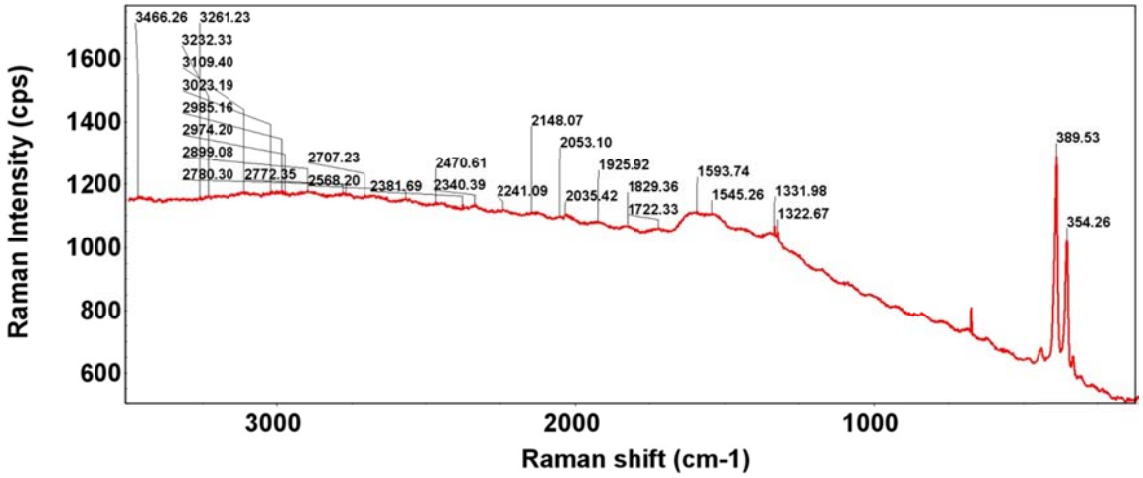

Figure 34. Micro diamond peaks can be seen at 1331.98 cm^{-1} and 1322.67 cm^{-1}. The peaks formed at 354.26 cm^{-1} and 389.53 cm^{-1} are due to the presence of the garnet host.

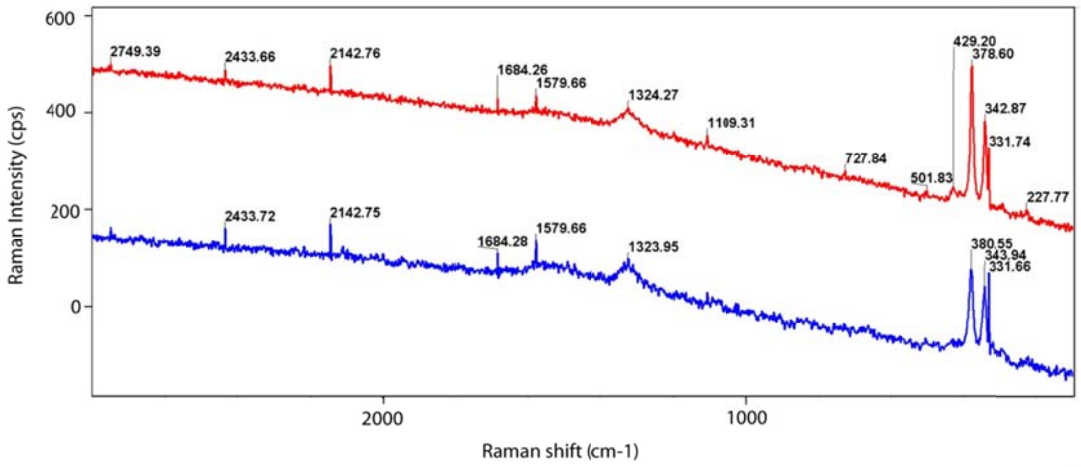

Figure 35. Micro diamond peaks are observed at 1324.27 cm^{-1} (red) and 1323.95 cm^{-1} (blue)

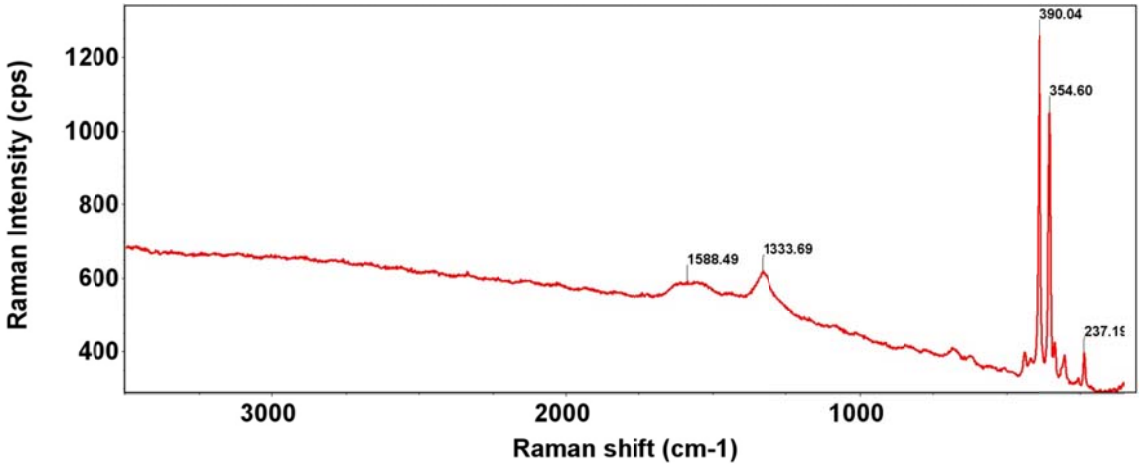

Figure 36. Garnet peaks were detected at 354.60 cm^{-1} and 390.04 cm^{-1}, whereas a micro diamond peak was observed at 1333.69 cm^{-1}

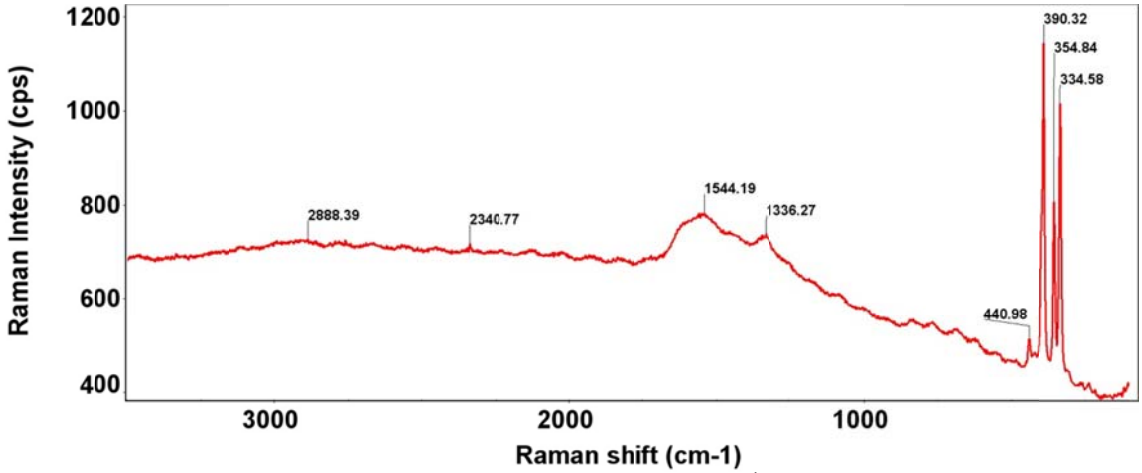

Figure 37. One micro diamond peak is located at 1336.27 cm^{-1}

6.3.2 Micro Diamonds in Micro Cracks within Garnet Crystals

The micro diamond shifts found in these samples shows peaks at 1322 cm^{-1} and/or about 1331 cm^{-1}. However, these peaks are noticeably smaller that the micro diamond peaks found in the garnet crystals. They are also narrower than the abovementioned peaks.

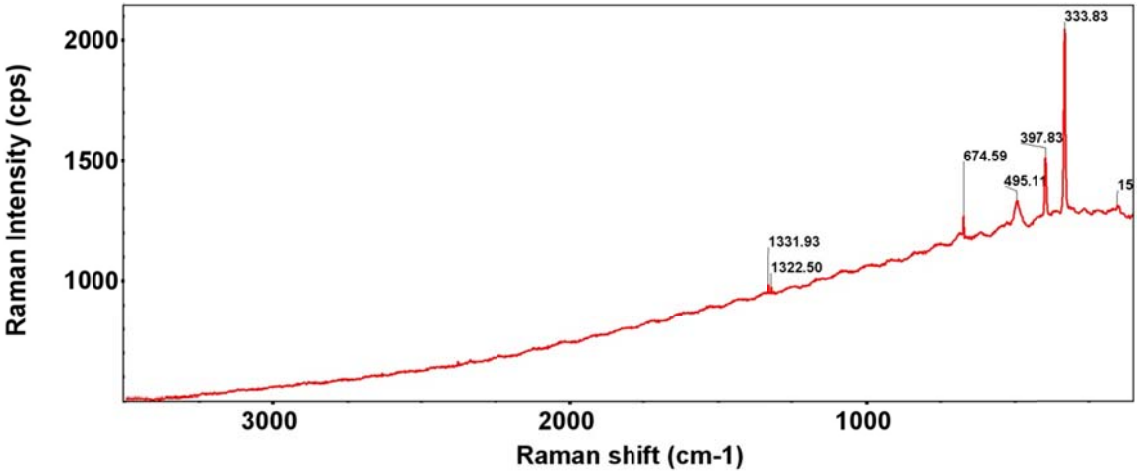

Figure 38. Peaks were detected at 1331.93 cm^{-1} and 1322.50 cm^{-1}. These are indicative for micro diamonds

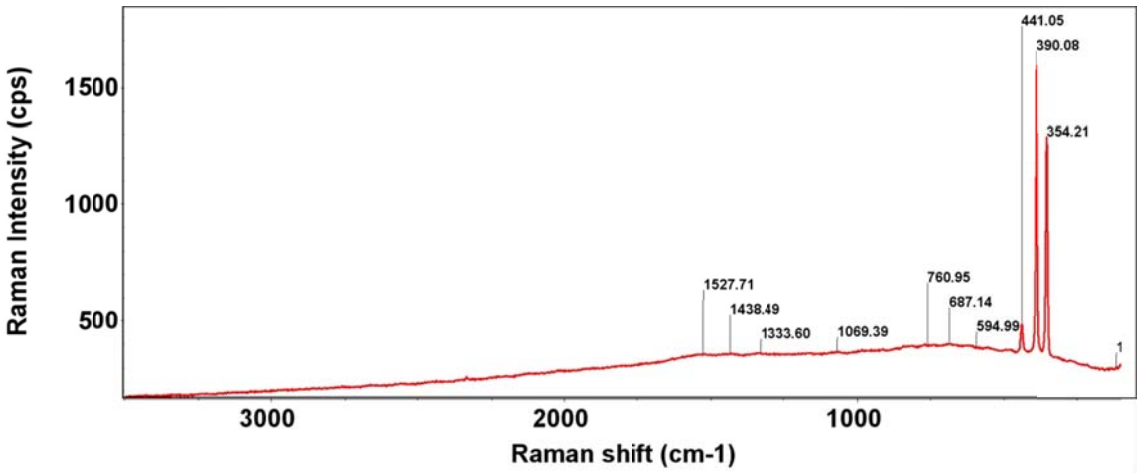

Figure 39. Only one micro diamond peak is observed at 1333.60 cm^{-1}

6.3.3 Micro Diamonds in Serpentine Veins

Two micro diamond Raman peaks were observed in the serpentine vein samples. These peaks were located at about 1322 cm^{-1} and 1331 cm^{-1}. These peaks are also smaller and narrower than the micro diamond peaks measured in the garnet crystals. The other peaks that can be observed in figures 40 and 41 were caused by the surrounding serpentine minerals.

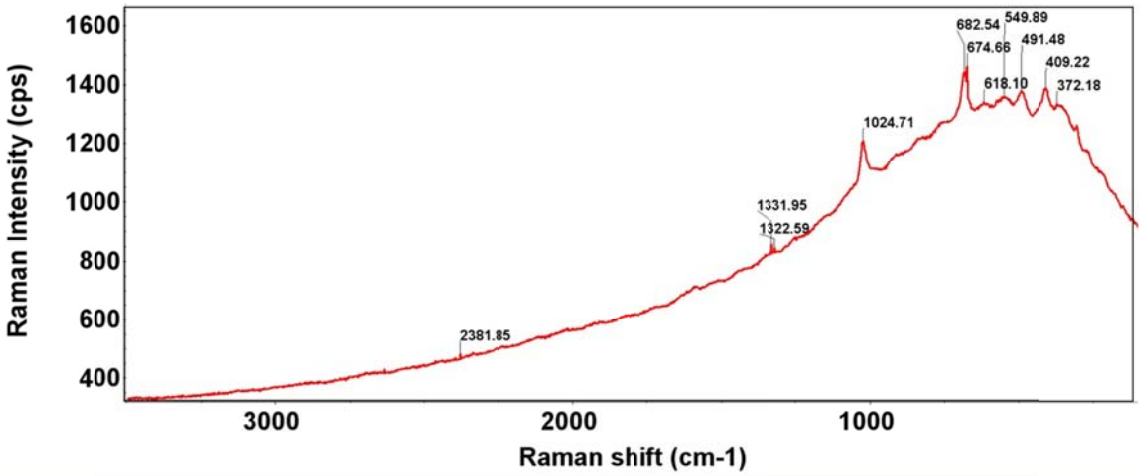

Figure 40. Micro diamond peaks were detected at 1331.95 cm^{-1} and 1322.59 cm^{-1} respectively

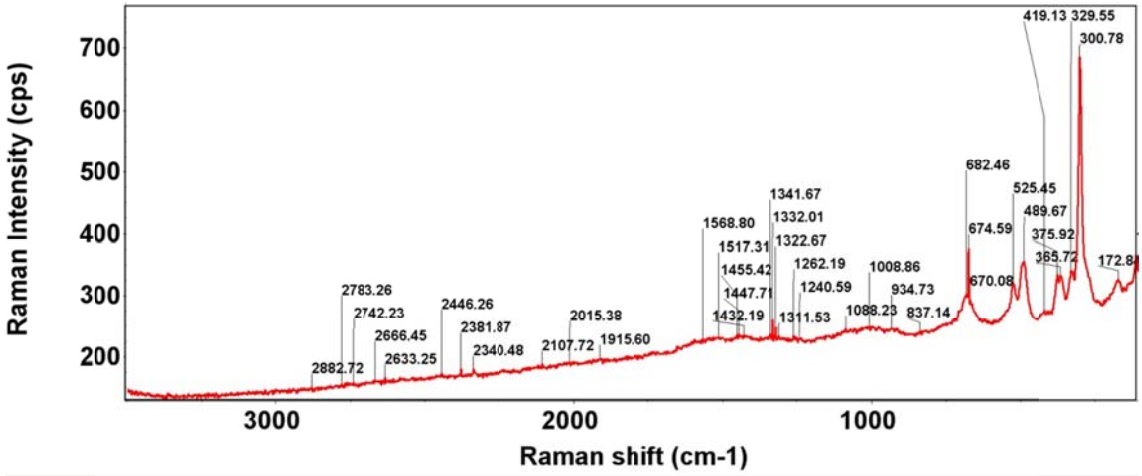

Figure 41. Two micro diamond peaks are also seen at 1332.01 cm^{-1} and 1322.67 cm^{-1}

6.4 Conclusion

The micro diamonds that were observed in the garnet crystals shows peaks at about 1322cm^{-1} and 1332 cm^{-1} . These peaks are large as well as wide. The micro diamonds are considered to be high pressure diamonds formed by polymorphic phase transition processes that occur in the diamond window. These high pressure micro diamonds have two crystallographic systems thus leading to the detection of these two micro diamond peaks.

Micro cracks that occur in cracks within garnet crystals were also measured. The Raman peaks caused by the micro diamonds found in these cracks are smaller and narrower than the peaks formed by the micro diamonds in the garnet crystals. The same observation was also made for the peaks formed by the micro diamonds present in the serpentine veins. These micro diamonds are always surrounded by serpentine. Since these serpentine minerals are formed close to the earth's surface at low pressures and the peaks from the serpentine vein and the micro cracks are similar, it suggests that they were formed by the same processes at the same pressure and temperature conditions as well as at a similar time.

These results thus show that at least two generations of micro diamonds, one high pressure modification and one low pressure modification, were identified in the studied eclogite sample. The high pressure micro diamonds were formed by polymorphic phase transition of graphite into diamond. This process occurs in the diamond window (Fig. 4). The low pressure modification on the other hand is formed by polycondensation processes caused by the formation of serpentine, which controls the C:O:H ratios in the fluid thus leading to the formation of micro diamonds by the presence of chemical reactions.

Chapter 7: Volatiles around Totally Embedded Micro Cracks

7.1 Introduction

Earth is considered to be a water planet. The surface processes of the planet are dominated by oceans of liquid water. The water on the planet's surface controls weathering processes as well as sediment transport and deposition. In the interior, water fluxes melting and controls the solid-state viscosity of the convecting mantle and thus controls volcanism and tectonics. Oceans cover 70% of the earth's exterior but it only makes up about 0.025% of the planet's mass. Hydrogen is the most abundant element in the cosmos but it is one of the most poorly constrained chemical compositional variables in the bulk earth (Keppler and Smyth, 2006).

The earth's crust and mantle partly consist of nominally anhydrous minerals and a large amount of these minerals can incorporate assessable quantities of hydrogen. Nominally anhydrous minerals are minerals that contain oxygen as the major anion, the principal incorporation mechanism is hydroxyl, OH-, and the chemical component is equivalent to water, H_2O. The hydrogen proton is a monovalent cation, even though it does not occupy the same structural position in a mineral structure as a normal cation. The hydrogen proton rather forms a bond with the oxygens on the edge of the coordination polyhedron. The amount of hydrogen incorporated into the structure is sensitive to pressure changes and thus increases with pressure and sometimes temperature. The solubility of hydrogen in nominally anhydrous minerals is thus much more sensitive to pressure and temperature changes than that of other elements (Keppler and Smyth, 2006).

The amount of hydrogen incorporated into the nominally anhydrous phases in the mantle rocks may constitute the largest water reservoir in the planet. This is due to the fact that the mass of rocks in the interior is much larger than the mass of the oceans. Understanding the behaviour and chemistry of hydrogen in minerals at the atomic scale is thus critical in understanding the geology of the planet. Advances in measurement, detection and location of hydrogen in the nominally anhydrous oxide and silicate minerals that compose the planet, have been made in recent years. There have also been advances in experimental methods for measurement of hydrogen diffusion and the effects of hydrogen on the phase boundaries and physical properties whereby the presence of hydrogen in the interior may be inferred from seismic or other geophysical studies (Keppler and Smyth, 2006).

To further understand the importance, location and diffusion profiles of hydrogen in the mantle, eclogites from the Roberts Victor mine have been studied. Eclogites can act as water and CO_2 reservoirs (Potgieter, 2009). The water and CO_2 is found on one-dimensional defects such as point defects and two-dimensional defects such as cracks and monomineralic and interface grain boundaries (Sommer et al., 2008). These defects are found in garnets and omphacites, which are the rock-forming minerals in the studied eclogite. Water has a major influence on the ductile-brittle regime in the Earth's mantle (Regenauer-Lieb et al., 2001). A problem that exists in quantifying water and CO_2 concentrations is the necessary high spatial resolution in nanoscale, which is needed for doing measurements of volatiles on point defects. Therefore the exact mechanism of water and CO_2 located on point defects cannot be observed directly. Heggie (1992) described the pumping of water along two-dimensional defects such as cracks and grain-boundaries which are enhanced through deformation. The basics of this process were described by Griggs (1967) and is called hydrolytic weakening.

Hiraga (2004) has found, that the water concentration in the direction of grain-boundaries, are characterized by the increase of incompatible elements towards the grain-boundary. The increase of water in the direction of monomineralic and interphase grain boundaries was described recently (Sommer et al., 2008). These authors used Synchrotron based FT-IR, because normal bench-top FT-IR equipment has a too low sensitivity and spatial resolution to detect water towards grain boundaries. A second problem in quantifying water and CO_2 concentration in minerals is that during the eruption of the eclogite from the earth's mantle to the surface, water and CO_2 can be added or removed, depending of the solubility of volatiles in the kimberlitic melt.

These problems have been solved by measuring volatiles in totally embedded monomineralic grain boundaries in garnets of the studied eclogites. Conventional bench top FT-IR microscopes have an unfavourable trade-off between the brilliance of the IR source and the analysed size of the measured area. This problem has been overcome by using synchrotron based FT-IR. The ANKA synchrotron at the Forschungszentrum Karlsruhe, Germany, with a defraction-limited IR edge-radiation from its 2.5 GeV, 200mA beam has been used for the measurements.

7.2 Analytical Methods

The studied samples E18, E19 and E24 are double polished thick sections from the eclogite xenolith (Fig. 6). Totally embedded micro cracks in garnet and serpentinized monomineralic and interphase grain boundaries were studied by using a petrographic microscope as discussed in chapter 3.

The micro cracks in the garnet were studied by using thick sections, which have been polished on both surfaces in paraffin to avoid any contamination with molecular water. The crystallographic orientation was neglected due to the cubic nature of the garnet. The thickness of the analysed double polished sections is 65 μm. The Beer-Lambert law was used to calculate the water content from the FT-IR spectra. An absorption coefficient 0.7194 was used to determine the water content in the garnet grains (Bell and Rossman., 1992). The OH peak was normalized to 1 cm. The study focused on totally embedded micro cracks and serpentinized grain boundaries. Totally embedded micro cracks from the sub-grain boundaries were selected. These fully embedded cracks were selected to avoid any interference from surface cracks or intersections with the polished surfaces of the garnet grain.

The fully embedded cracks were investigated with FT-IR in transmitted-light mode. IR absorption spectra in the range from 600 to 10000 cm^{-1} were acquired at the infrared beam line of the ANKA synchrotron with incident light polarized using a Bruker IFS 66v/S spectrometer coupled to an IRscopeII microscope with a 36x, 0.5 N.A. Schwarzschild objective and a liquid-N_2 cooled MCT detector. The spectral region of interest for this study is the OH stretching range at around 3780 cm^{-1}. Brilliance advantage (photon flux per unit source area into unit emission angle) of synchrotron light compared to conventional sources was exploited, which allows much higher measurement beam intensity through small sample areas. In addition to the single-spot measurements the synchrotron infrared light of ANKA was used to analyse large numbers of overlapping spots using a step size of 2 μm and an aperture of 4 μm diameter in a grid pattern accessed by an automated X-Y stage.

7.3 OH and CO_2 Distribution Along Totally Embedded Micro Cracks

7.3.1 Correlation of OH and CO_2 Distribution Profiles

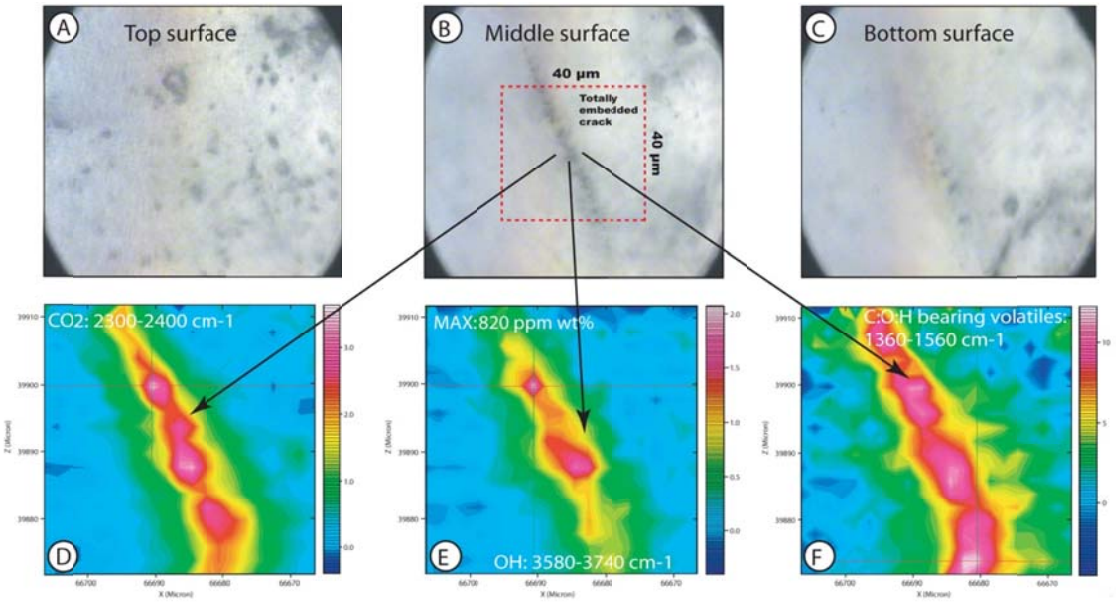

Figure 42. Two dimensional maps showing the distribution of OH, CO_2 and other volatiles in the studied garnets. A: The top surface of the garnet sample, B: Middle surface containing a micro crack as well as micro diamonds from sample E18, C: Bottom surface of the studied garnets, D: CO_2 diffusion profile, E: OH diffusion profile and F: diffusion profile of other volatiles present around the crack. All maps are 40x40 µm in size and consist of 21x21 measurements with a stepwise of 2 µm and 512 scans (Potgieter, 2009).

The analysed garnet from sample E18 shows totally embedded micro cracks in the garnet with inclusions of micro diamonds in the studied crack (Fig. 42b). The synchrotron infrared light of ANKA was used to analyse 512 scans of overlapping spots using a step size of 2 µm and an aperture of 4 µm in diameter in a grid pattern accessed by an automated X-Y stage. The size of the analysed map is 40 x 40 µm (Fig. 42b). The background was measured on a dry area in the garnet. The investigated micro crack is approximately 40 µm long and has an opening of about ~ 5-10 nm (Figs. 42b). This crack does not crop out at the top or bottom surface (Figs. 42a & 42c). In figure 42b small inclusions of micro-diamonds can be observed inside the crack. The zone around the crack forms spots of C:O:H bearing volatiles (Figs. 42d, 42e, 42f). These wet clouds are about 20 microns in diameter and the peak at ~ 3700 cm^{-1} is

indicative of the peak shift of OH in the garnet located in the crystal lattice towards the crack (Fig. 42b).

Two peaks were observed in the studied garnets, one at 3700 cm^{-1} which is suggestive of the hydro grossular component in the garnet and the second is another at 3655 cm^{-1} which is typical for the pyrope component in the investigated garnet (Fig. 42b). The peak at 3700 cm^{-1} becomes more intensive at the totally embedded crack. The OH concentration in the wet clouds is up to 10x higher and is up to 820 ppm (Fig. 42b).

CO_2 concentration around the same micro crack was also measured. At ~2350 cm^{-1} a strong CO_2 band can be observed (Figs. 42a and 43a) The CO_2 distribution around the crack shows nearly the same pattern as the OH distribution and shows similar diffusion rates around the investigated crack (Figs. 42a & 42b). Strong signals have been found between 1360 cm^{-1} and 1560 cm^{-1} in the wavelength bonds (Fig. 42c). These wavelengths bonds can be allocated to those of CO, CH_4, CH_2O and CH_3OH (Fig. 42c and 43c). The wavelength at 1423 cm^{-1} of the FTIR spectra, and the Raman shift at 1324 cm^{-1} are indicative for micro-diamonds (Fig. 42c). The distribution pattern of CO, CH_4, CH_2O and CH_3OH is the same as those of OH and CO_2 (Figs. 42d, 42e, 42f).

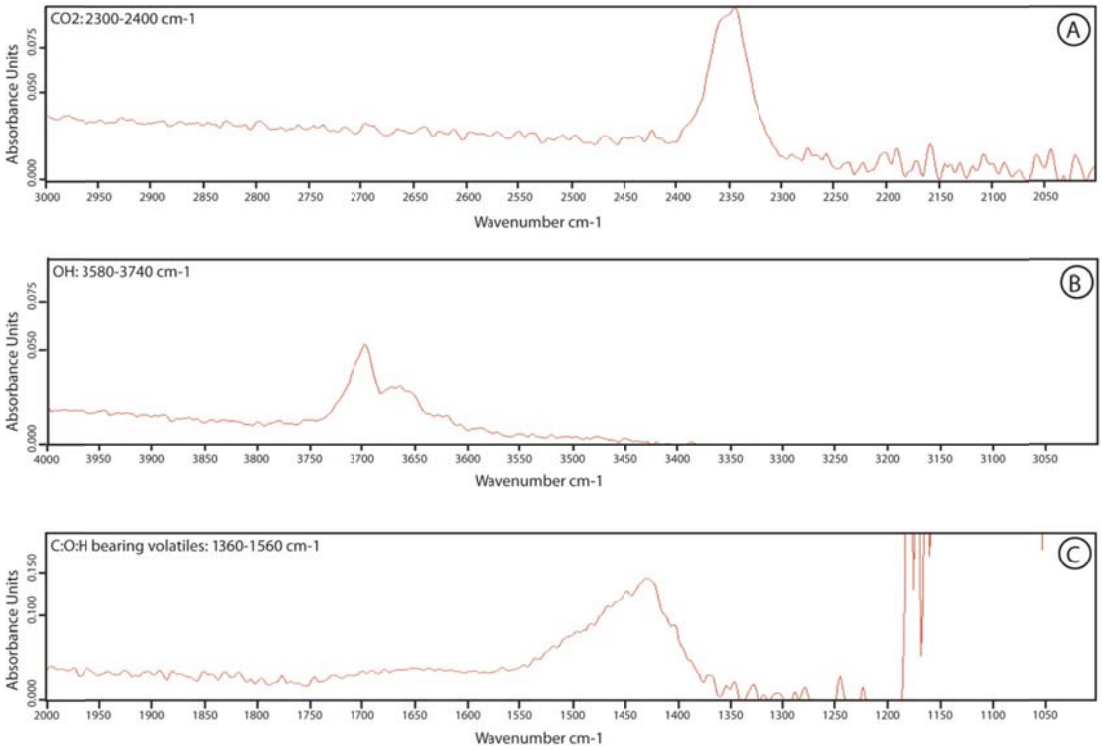

Figure 43. A: CO_2 peak at 2300 – 2400 cm^{-1}, B: OH peak at 3580 – 3740 cm^{-1} and C: C:O:H bearing volatile peak at 1360 – 1560 cm^{-1}. Examples of C:O:H bearing volatiles are CO, CH_4, CH_2O and CH_3OH (Potgieter, 2009)

7.3.2 Non-correlation of OH and CO_2 Distribution Profiles

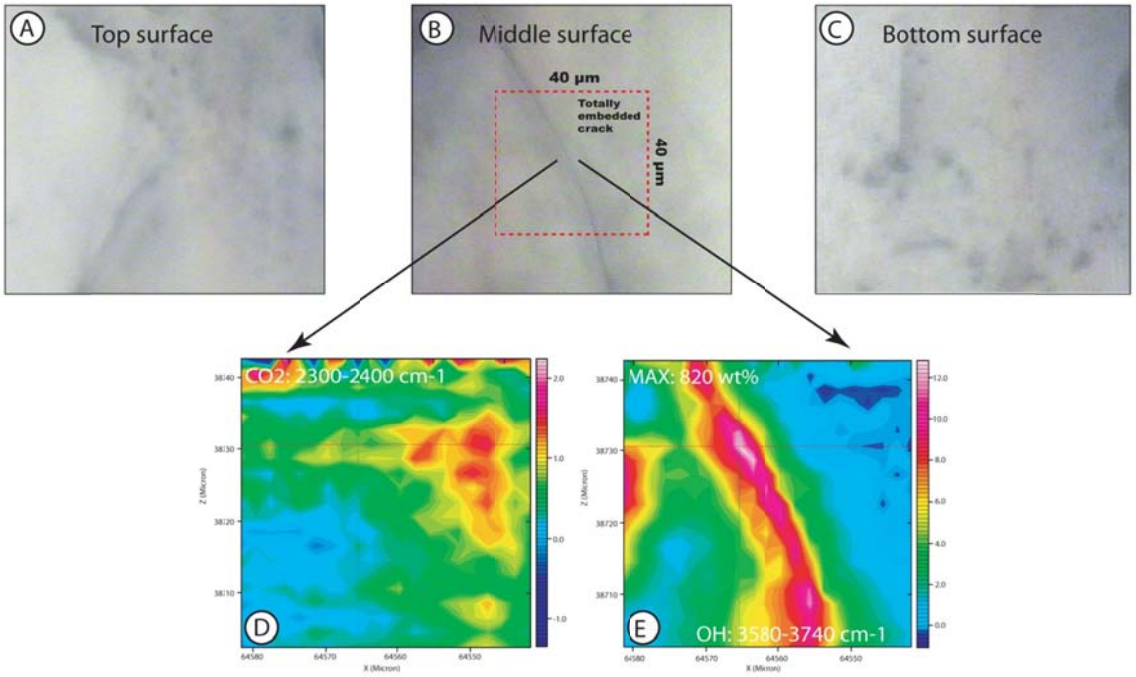

Figure 44. Two dimensional maps showing the distribution of OH and CO_2 in the studied garnets of sample E19. A: The top surface of the garnet sample, B: Middle surface containing a micro crack as well but no micro diamonds, C: Bottom surface of the studied garnets, D: CO_2 diffusion profile, E: OH diffusion profile. All maps are 40x40 µm in size and consist of 21x21 measurements with a stepwise of 2 micron and 512 scans (Potgieter, 2009).

The studied garnet grain in sample E19 shows totally embedded, inclusion free, micro cracks (Fig. 44b). The same analytical setup was used as in the measurement of sample E18. The investigated micro crack is approximately 60 µm long and has an opening of between ~ 5-10 nm (Fig. 44b). The investigated sample is also a totally embedded crack as in sample E18 (Figs. 44a, 44b & 44c). "Spots" of volatiles can be observed in the micro crack (Figs. 44d & 44e). These OH "clouds" are also found to be parallel to the crack and are approximately 25 µm wide (Fig. 44e). The location of the peak at ~ 3700 cm^{-1} is indicative of the peak shift of OH located in the crystal lattice at the crack.

As in sample E18, two peaks could again be identified. A hydro grossular peak at 3700 cm^{-1} and a pyrope peak at 3655 cm^{-1} were found. As in sample E18 the peak at 3700 cm^{-1} becomes more intensive at the embedded crack. The OH concentration in the wet clouds is again up to 10x higher (Fig. 44e).

Measurements were also done on the CO_2 concentration around the micro crack. A strong CO_2 band can be observed at ~2350 cm^{-1}. The CO_2 distribution around the embedded crack does not show any correlation with the OH distribution, which was the case in sample E18 (Figs. 42d & 42e).

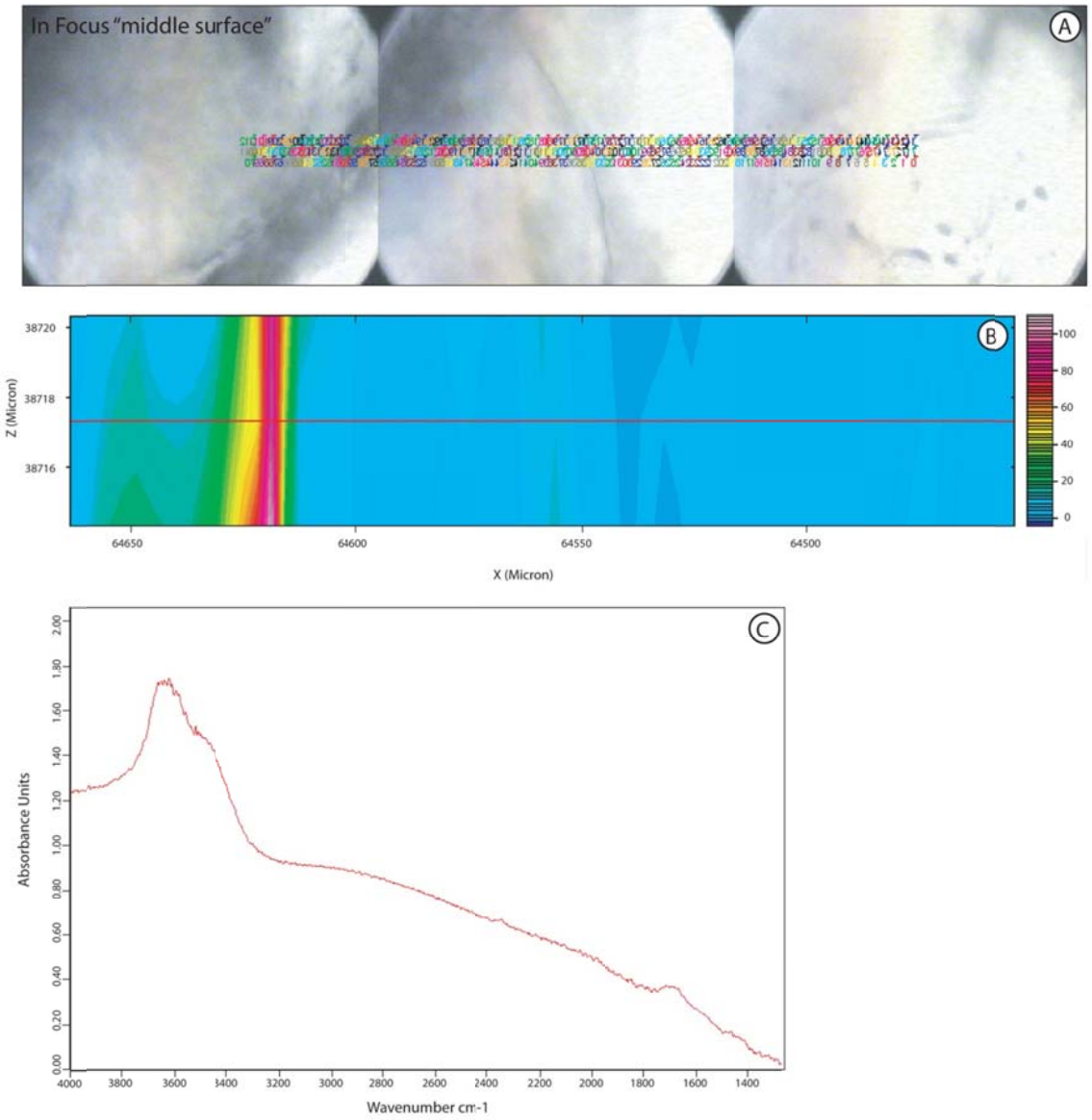

Figure 45. OH profile measured over a distance of 220 µm X 6 µm of a micro crack of sample E24. The figure shows that OH is located in two-dimensional defect structures which act as mono mineralic and interface structures and does not occur in the crystal lattice.

A profile of about 220 μm was measured at the garnet grain of sample E24. This profile was measured at the lower middel section of the studied rock sample (Fig.7). 256 scans of overlapping spots were made to construct the profile over the totally embedded crack in the garnet (Fig. 45a). A step size of 3 μm and an aperture of 4 μm in diameter in a grid pattern accessed by an automated X-Y stage were used (Fig. 45a). The size of the analysed profile is 220 x 10 μm (Fig. 45a). The background was again measured on a dry area in the garnet. This micro-crack is 60 μm long and is about ~10 nm wide (Figs. 45a). The investigated crack does not crop out at the top or bottom surface and is thus totally embedded (Figs. 45a). The OH is located at the 2-dimensional defect structure at a wavelength of ~ 3700 cm^{-1} (Figs. 45b & 45c). The carbon bearing volatiles such as CO_2, CO, CH_4, CH_2O and CH_3OH could not be detected.

7.4 Diffusion Profiles

The OH diffusion profiles were calculated around totally embedded micro cracks within garnet crystals located in the studied eclogite. The diffusion can only be calculated for OH due to the fact that no experimental data exists for the other volatiles found in the sample. Figure 42e was used to measure the OH diffusion profile.

OH diffusion profiles are calculated in order to obtain information about the ascent rate of the kimberlite carrying the eclogitic samples. This is done by making use of the equation from Ingrin and Blanchard (2006) as well as the data set from Kurka et al (2005).

Calculations for the garnet matrix and the centre of the micro crack were made. OH concentration of about 820 ppm wt% was detected in the centre of the studied micro crack while calculations for the garnet matrix yielded an OH concentration of about 15 ppm wt% .

OH diffusion profiles have been constructed around these micro fractures which extend up to 50 micron in to the garnet matrix. Round OH clouds were also observed around the micro cracks (Sommer., 2009*a*).

The calculated diffusion time varies between 10 minutes and a couple of hours, depending on the temperature used for the calculation. For example: by using a temperature of 1250°C, the diffusion process will last about 10 minutes

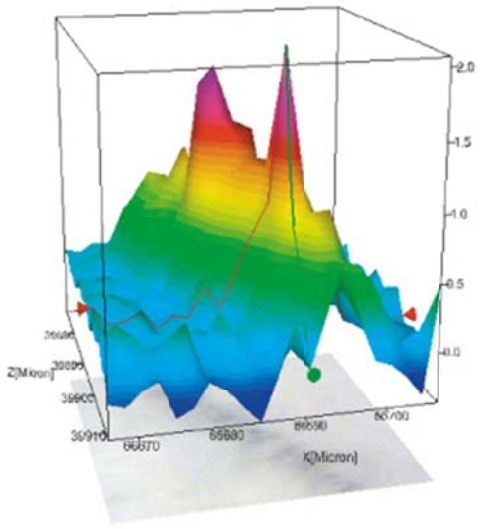

Figure 46. 3D plot of an OH profile from the studied garnet

7.4 Conclusion

Totally embedded micro cracks in the garnet crystals have been analysed using Synchrotron based FT-IR at ANKA in Karlsruhe, Germany. These totally embedded micro cracks contain C:O:H bearing volatiles represent remnants and the last snapshot of C:O:H bearing volatiles in the studied garnets.

If the OH, CO_2 and the C:O:H bearing fluids correlate with each other in a specific micro crack, micro diamonds are likely to be found inside the analysed micro crack (Fig.42). If the OH and the CO_2 do not correlate with each other, the C:O:H bearing fluids cannot be detected and micro diamonds will not be found inside the micro cracks (Fig.44). If the OH occurs alone, it is likely that no C:O:H-bearing fluid will be detected (Fig.45.).

The OH diffusion profiles around totally embedded micro cracks are indicative of ultra-sonic uplift of the xenoliths within the kimberlitic melt from the Earth´s upper mantle to the surface. According to Sommer (2009*a*), if the temperature is ~1250°C and the pressure ~50kbar, the whole eruption process may take as little as 10 minutes, but when the temperature is lower, the speed of the kimberlite eruption slows down.

Chapter 8: Discussion and Conclusion

A large number of experiments support the idea that C:O:H bearing volatiles can lead to polycondensation of light carbon bearing molecules and to the formation of micro diamonds at low pressure conditions. This is in direct contrast to the idea that all diamonds are formed by a high pressure graphite-diamond phase transition in the diamond window. These experiments also show that the synthesis of diamonds through polycondensation takes place at a certain C:O:H ratio as seen in the volatile "clouds" around two-dimensional defects in eclogitic garnets from the Roberts Victor mine in South Africa. The results give new evidence that natural micro diamonds can be formed under low to medium pressures. This process may even take place close to the Earth´s surface. These findings are in agreement with the observations from Rudenko et al., 1993 and Rudenko and Kulakova 1996. These authors conducted experimental studies on the formation of micro diamonds under low pressure conditions through polycondensation of carbon-bearing molecules in cracks and grain boundaries. Polycondensation of carbon molecules may produce micro diamonds at low pressure conditions, but only under favorable conditions when the correct C:O:H ratio causes carbon bearing chemical reactions.

Three types of micro diamonds were found in the eclogite sample by using Raman analysis. They are micro diamonds in the matrix, micro diamonds in the micro cracks and micro diamonds in serpentine veins. These micro diamond types show different Raman peak shifts that might be caused by crystallographic differences in the micro diamonds. The micro diamonds in the garnet matrix exhibits large, wide peaks that might indicate high pressure diamonds with cube and cube-octahedral crystallographic systems. The micro diamonds found in the micro cracks and within the serpentine veins on the other hand, display small, narrow Raman peaks that might have been formed by low pressure conditions close to the earth's surface.

The volatiles around two-dimensional defect structures such as micro cracks within the garnet crystals have been analysed. Three different garnet crystals from a metasomatised eclogite from the Roberts Victor mine in South Africa were investigated. It was found that the distribution pattern of CO, CH_4, CH_2O and CH_3OH (C:O:H) is the same as those of OH and CO_2 (Figs. 42d, 42c, 42e). In these cases where there is a correlation between all the volatiles it is likely that micro diamonds will be found within these micro cracks. Where the OH and

CO_2 do not correlate with each other, the C:O:H bearing fluids are also not detectable and no micro diamonds will be observed (Fig. 44d & 44e).

It is concluded that micro diamonds only occur in the micro cracks where all the measured volatile profiles show the same distribution pattern as seen in sample E18 (Figs, 42d, 42c, 42e). It was found that the micro diamonds occurring in the micro cracks will only form at a favourable C:O:H ratio. These results support the findings of Rudenko et al., 1993, which states that micro diamonds may be formed due to the polycondensation of light carbon molecules.

References

Allsopp H.L. & Barrett D.R., 1975. Rb–Sr determinations on South African kimberlite pipes. Physics and Chemistry of the Earth 9: 615–617.

Arima M. & Kozai Y., 2008. Diamond dissolution rates in kimberlitic melts at 1300-1500 degrees C in the graphite stability field. European Journal of Mineralogy, V. 20/3: 357-364.

Bachmann P.K., Leers D. & Lydt H., 1991. Diamond and Related Materials 1 (1) p.12,

Bell D.R & Rossman G.R., 1992. Water in the Earth's mantle: The role of nominally anhydrous minerals. Science 255: 1391–1397.

Boyd, F.R. & Gurney, J.J., 1986. Diamonds and the African lithosphere, Science, v. 232, p. 472-477.

Bucher K., 2002. Introduction to Mineralogy and Petrology, University of Freiburg, Department for Mineralogy, Petrology and Geochemistry, Freiburg im Breisgau, Germany

Deer, W.A., Howie, R.A. & Zussman, J., 1992.An Introduction to the Rock Forming Minerals. Longman Scientific and Technical.

Fedortchouk Y., Canil D. & Carlson J.A., 2005. Dissolution forms in Lac de Gras diamonds and their relationship to the temperature and redox state of kimberlite magma. Contribution to Mineralogy and Petrology, V. 15/1: 54-69.

Fedortchouk Y. & Canil D, 2009. Diamond oxidation at atmospheric pressure: development of surface features and the effect of oxygen fugacity. European Journal of Mineralogy, V. 21/3: 623-635.

Field M., Stiefenhofer J, Robey J. & Kurszlaukis S., 2008. Kimberlite-hosted diamond deposits of southern Africa: A review. Ore Geology Reviews: 34:33-75

Griffin W.L., O'Reilly S.Y., Natapov L.M. & Ryan C.G., 2003b. The evolution of lithospheric mantle beneath the Kalahari Craton and its margins. Lithos 71: 215–251.

Griggs D.T., 1967. Hydrolytic weakening of quartz and other silicates. Geol J Royal Astron Soc 14: 19–32.

Gurney J.J., Helmstaedt H. & Moore R.O., 1993. A review of the use and application of mantle mineral geochemistry in diamond exploration. Pure & Appl.Chem. Vol.65, 12: 2423-2442.

Gurney J.J. & Kirkley M.B., 1996. Kimberlite dyke mining in South Africa. Africa Geoscience Review 3: 191–201.

Haggerty S.E., 1986. Diamonds and the African lithosphere, Macmillan Magazines LTD, Porters South, 4 Crinan St, London, England N1 9XW, v. 320: 34-37.

Heggie M., 1992. A molecular water pump in quartz dislocations. Nature 355: 337-339.

Hiraga T., Anderson I.M. & Kohlstedt D.L., 2004. Grain boundaries as reservoirs for incompatible elements in the Earth's mantle. Nature 427: 699-703.

Ingrin J. & Blanchard M., 2006. Diffusion of Hydrogen in Minerals, Chapter 13: 291-320.

Keppler H. & Smyth J.R., 2006. Water in nominally anhydrous minerals. Reviews in mineralogy and geochemistry 62: v-vi.

Kurka A., Blanchard M. & Ingrin J., 2005. Mineralogical Magazine Volume: 69 Issue: 3: 359-371.

Melissa B., Kirkley J.J., Gurney M.L., Otter S. J. & Hill L.R., 1995. The application of C isotope measurements to the identification of the sources of C in diamonds: a review, 6: 477-494.

Mitchell R.H., 1986. Kimberlites. Mineralogy, geochemistry and petrology. Plenum, New York. 442.

Mitchell R.H., 1995. Kimberlites, orangeites, and related rocks. Plenum Press, New York. 410.

Posges G., 2005. Meteoritics and Planetary Volume: 40 Issue: 9-10: 1555-1557.

Potgieter J., 2009. OH and CO2 diffusion profiles in garnets from eclogitic xenoliths from the Rovic diamond mine, South Africa. Unplublished Honours thesis.

Regenauer-Lieb K., Yuen D. & Branlund J., 2001. The initiation of subduction: criticality by addition of water? Science 294: 578–580.

Roper S.M. & Lister J.R., 2007. Buoyancy-driven crack propagation: the limit of large fracture toughness. Journal of Fluid Mechanics, V. 580: 359-380.

Rossmann G.R. & Aines R.D., 1991. The hydrous components in garnets – grossular – hydrogrossular. American Mineralogist. V. 76/7-8: 1153-1164.

Rudenko A.P. & Kulakova I.I., 1993. The chemical synthesis of diamond. Aspects of the general theory. Russian Chemical Reviews. 62: 87-104.

Rudenko A.P. & Kulakova I.I., 1996. Formation of diamond nuclei under the growth of films and crystals from the gas phase. Diamond and Related Materials 5: 1070-1073.

Sheahan P.A. & Cherry M.E., 1993. Ore Deposit Models Volume II. Geological Association of Canada; ISBN-10: 0-919216-50-1; ISBN-13: 978-0-919216-50-1; ISSN: 0821-381X.

Skinner E.M.W., 1989b. Contrasting Group 1 and Group 2 kimberlite petrology: towards a genetic model for kimberlites. In: Ross J., Jacques A.L., Ferguson J., Green D.H., O'Reilly S.Y., Danchin R.V., Janse A.J.A. (Eds.), Kimberlites and Related Rocks, Volume 1. Proceedings of the Fourth International Kimberlite Conference. Geological Society of Australia Special Publication 14, Perth, Australia,528–544.

Smith C.B., Allsopp H.L., Kramers J.D., Hutchinson G. & Roddick J.C., 1985. Emplacement ages of Jurassic–Cretaceous South African kimberlites by the Rb–Sr method on phlogopite and whole-rock samples. Transactions of the Geological Society of South Africa 88: 249–266.

Sommer H., Regenauer-Lieb K., Gasharova B. & Siret D., 2008. Grain boundaries: possible water reservoir in the Earth's mantle? Mineralogy and Petrology, 94: 1-8.

Sommer H., 2009*a*. "Wet" low angle subduction: a possible mechanism below the Tanzania craton 2 Ga ago. Mineralogy and Petrology, 96: 113-120.

Sommer H., Regenauer-Lieb K., Gaede O., 2009*b*. Weertman cracks and the fast extraction of diamonds from the Earth's mantle (UNESCO IGCP 557) Goldschmidt Conference Davos. Geochimica and Cosmochimica Acta, 73, A1249-A1249

Sparks R.S.J., Baker L. & Brown R.J., 2006. Dynamical constraints on kimberlite volcanism. Journal of Volcanology and Geothermal Research, V. 155/1-2: 18-48.

Spear F.S., 1993. Metamorphic Phase Equilibria and Pressure-Temperature-Time Paths. Mineralogical Society of America MONOGRAPH.

Spence D.A. & Turcotte D.L., 1990. Buoyancy - driven magma fracture - a mechanism for ascent through the lithosphere and the emplacement of diamonds. Journal of Geophysical Research -Solid Earth and Planets, V. 95/B4: 5133-5139.

Takada A., 1990. Experimental - study on propagation of liquid - filled crack in gelatin - shape and velocity in hydrostatic stress condition, Journal of Geophysical Research - Solid Earth and Planets, V. 95/B6: 8471-8481.

Wagner P.A., 1914. The diamond fields of South Africa. Transvaal Leader, Johannesburg. 347.

Weertman J., 1971*a*. Theory of water - filled crevasses in glaciers applied to vertical magma transport beneath oceanic ridges. Journal of Geophysical Research, V. 76/5: 1171-1174.

Weertman J., 1971*b*. Velocity at which liquid–filled cracks move in Earth's Crust or in Glaciers. Journal of Geophysical Research, V. 76/35: 8544-854.

Acknowledgements

I would like to express my sincere gratitude to the following people:

Dr Holger Sommer, who is my supervisor, for his valuable advice and encouragement, Professor Wayne Colliston and Professor Klause Regenauer-Lieb for their helpful suggestions, Professor Haemyeong Jung for the opportunity to visit the Seoul National University, Biliana Gasharova for the work she has done on the OH synchrotron measurements and finally, Hardy, my mother, Bertus and my grandmother for their loyal support.

Appendix

Only the representative microprobe analyses are shown in tables 1 to 7. The atomic units were calculated by estimating that all the Fe used is 2^{+}.

The information used for the garnet profile and the synchrotron based FT-IR analysis are electronically available from myself or Dr Holger Sommer.

Jessika Potgieter: jessikapotgieter@yahoo.com

Dr Holger Sommer: somhol@yahoo.de

Table 1

	vm_bt12	vm_cpx13	vm_cpx14	vm_cpx15	vm_cpx16
wt %					
SiO2	37.84	52.42	52.00	54.08	54.01
TiO2	2.66	0.34	0.42	0.35	0.54
Al2O3	16.88	1.95	3.07	3.50	3.30
Cr2O3	0.18	0.14	0.24	0.17	0.24
BaO	0.00	0.00	0.00	0.00	0.00
FeO	10.50	7.00	7.51	5.73	5.87
MnO	0.14	0.14	0.29	0.11	0.17
MgO	18.40	17.07	16.84	14.80	14.70
CaO	0.02	18.57	17.63	17.74	17.79
Na2O	0.66	0.68	0.74	2.69	2.50
K2O	9.34	0.00	0.00	0.00	0.00
ZrO2	0.00	0.00	0.00	0.00	0.00
SO3	0.00	0.00	0.00	0.00	0.00
Cl	0.00	0.00	0.00	0.00	0.00
F	0.00	0.00	0.00	0.00	0.00
Total	96.62	98.31	98.73	99.18	99.12
Ferrous Form	vm_bt12	vm_cpx13	vm_cpx14	vm_cpx15	vm_cpx16
Si	2.73	1.95	1.93	1.98	1.98
Al	1.43	0.09	0.13	0.15	0.14
Ti	0.14	0.01	0.01	0.01	0.01
Cr	0.01	0.00	0.01	0.01	0.01
Ba	0.00	0.00	0.00	0.00	0.00
Mg	1.98	0.95	0.93	0.81	0.80
Fe	0.63	0.22	0.23	0.18	0.18
Mn	0.01	0.00	0.01	0.00	0.01
Ca	0.00	0.74	0.70	0.70	0.70
Na	0.09	0.05	0.05	0.19	0.18
K	0.86	0.00	0.00	0.00	0.00
Zr	0.00	0.00	0.00	0.00	0.00
SO3	0.00	0.00	0.00	0.00	0.00
Cl	0.00	0.00	0.00	0.00	0.00
F	0.00	0.00	0.00	0.00	0.00
Sum	7.88	4.02	4.01	4.02	4.02

Table 2

	vm_cpx18	vm_am19	vm_cpx20	vm_cpx21	vm_cpx22
wt %					
SiO2	53.77	54.69	54.72	55.38	53.56
TiO2	0.39	0.40	0.30	0.34	0.42
Al2O3	3.36	5.56	5.64	5.60	2.70
Cr2O3	0.30	0.16	0.31	0.34	0.31
BaO	0.00	0.00	0.00	0.00	0.00
FeO	5.80	5.47	5.51	5.59	5.87
MnO	0.08	0.22	0.07	0.07	0.10
MgO	14.55	12.85	13.39	13.27	15.44
CaO	17.38	15.14	15.32	15.14	17.89
Na2O	2.82	4.29	4.10	4.05	2.29
K2O	0.00	0.17	0.12	0.18	0.00
ZrO2	0.00	0.00	0.00	0.00	0.00
SO3	0.00	0.00	0.00	0.00	0.00
Cl	0.00	0.00	0.00	0.00	0.00
F	0.00	0.00	0.00	0.00	0.00
Total	98.44	98.94	99.48	99.95	98.57
Ferrous Form	vm_cpx18	vm_am19	vm_cpx20	vm_cpx21	vm_cpx22
Si	1.99	2.00	1.99	2.00	1.98
Al	0.15	0.24	0.24	0.24	0.12
Ti	0.01	0.01	0.01	0.01	0.01
Cr	0.01	0.00	0.01	0.01	0.01
Ba	0.00	0.00	0.00	0.00	0.00
Mg	0.80	0.70	0.72	0.71	0.85
Fe	0.18	0.17	0.17	0.17	0.18
Mn	0.00	0.01	0.00	0.00	0.00
Ca	0.69	0.59	0.60	0.58	0.71
Na	0.20	0.30	0.29	0.28	0.16
K	0.00	0.01	0.01	0.01	0.00
Zr	0.00	0.00	0.00	0.00	0.00
SO3	0.00	0.00	0.00	0.00	0.00
Cl	0.00	0.00	0.00	0.00	0.00
F	0.00	0.00	0.00	0.00	0.00
Sum	4.03	4.03	4.03	4.02	4.03

Table 3

	vm_cpx23	vm_grt24	vm_cpx25	vm_bt26	vm_cpx27
wt %					
SiO2	54.96	40.94	51.46	43.36	53.83
TiO2	0.43	0.38	0.38	3.62	0.25
Al2O3	5.84	22.80	3.42	10.98	2.44
Cr2O3	0.07	0.14	0.27	0.06	0.20
BaO	0.00	0.00	0.00	0.00	0.00
FeO	5.58	15.47	8.03	8.54	5.72
MnO	0.25	0.65	0.24	0.06	0.17
MgO	12.69	15.61	16.72	19.63	15.18
CaO	14.99	4.88	17.59	0.00	18.10
Na2O	4.26	0.07	0.44	0.17	2.19
K2O	0.12	0.01	0.00	9.47	0.00
ZrO2	0.00	0.00	0.00	0.00	0.00
SO3	0.00	0.00	0.00	0.00	0.00
Cl	0.00	0.00	0.00	0.00	0.00
F	0.00	0.00	0.00	0.00	0.00
Total	99.19	100.95	98.54	95.88	98.07
Ferrous Form	vm_cpx23	vm_grt24	vm_cpx25	vm_bt26	vm_cpx27
Si	2.00	2.98	1.92	3.09	2.00
Al	0.25	1.95	0.15	0.92	0.11
Ti	0.01	0.02	0.01	0.19	0.01
Cr	0.00	0.01	0.01	0.00	0.01
Ba	0.00	0.00	0.00	0.00	0.00
Mg	0.69	1.69	0.93	2.09	0.84
Fe	0.17	0.94	0.25	0.51	0.18
Mn	0.01	0.04	0.01	0.00	0.01
Ca	0.58	0.38	0.70	0.00	0.72
Na	0.30	0.01	0.03	0.02	0.16
K	0.01	0.00	0.00	0.86	0.00
Zr	0.00	0.00	0.00	0.00	0.00
SO3	0.00	0.00	0.00	0.00	0.00
Cl	0.00	0.00	0.00	0.00	0.00
F	0.00	0.00	0.00	0.00	0.00
Sum	4.02	8.03	4.01	7.69	4.02

Table 4

	vm_cpx28	vm_cpx29	vm_cpx30
wt %			
SiO2	55.42	54.83	53.19
TiO2	0.41	0.41	0.31
Al2O3	5.81	5.69	2.44
Cr2O3	0.27	0.14	0.17
BaO	0.00	0.00	0.00
FeO	5.46	5.66	5.96
MnO	0.04	0.18	0.07
MgO	13.64	12.39	15.14
CaO	15.11	14.86	18.74
Na2O	4.19	4.31	1.76
K2O	0.18	0.10	0.01
ZrO2	0.00	0.00	0.00
SO3	0.00	0.00	0.00
Cl	0.00	0.00	0.00
F	0.00	0.00	0.00
Total	100.54	98.56	97.79
Ferrous Form	vm_cpx28	vm_cpx29	vm_cpx30
Si	1.99	2.01	1.99
Al	0.25	0.25	0.11
Ti	0.01	0.01	0.01
Cr	0.01	0.00	0.00
Ba	0.00	0.00	0.00
Mg	0.73	0.68	0.84
Fe	0.16	0.17	0.19
Mn	0.00	0.01	0.00
Ca	0.58	0.58	0.75
Na	0.29	0.31	0.13
K	0.01	0.00	0.00
Zr	0.00	0.00	0.00
SO3	0.00	0.00	0.00
Cl	0.00	0.00	0.00
F	0.00	0.00	0.00
Sum	4.02	4.01	4.01

Table 5

	vm_grt1	vm_grt2	vm_grt3	vm_grt4	vm_grt5
wt %					
SiO2	40.63	40.48	40.90	40.48	40.67
TiO2	0.33	0.40	0.40	0.27	0.29
Al2O3	22.16	21.89	22.30	22.22	21.66
Cr2O3	0.24	0.23	0.23	0.28	0.05
BaO	0.00	0.00	0.00	0.00	0.00
FeO	15.83	16.05	16.14	16.01	16.14
MnO	0.72	0.59	0.61	0.61	0.79
MgO	15.17	14.77	14.42	15.11	14.73
CaO	4.96	5.00	5.03	5.06	4.90
Na2O	0.08	0.09	0.12	0.37	0.11
K2O	0.00	0.01	0.02	0.06	0.01
ZrO2	0.00	0.00	0.00	0.00	0.00
SO3	0.00	0.00	0.00	0.00	0.00
Cl	0.00	0.00	0.00	0.00	0.00
F	0.00	0.00	0.00	0.00	0.00
Total	100.10	99.52	100.18	100.46	99.34
Ferrous Form	vm_grt1	vm_grt2	vm_grt3	vm_grt4	vm_grt5
Si	2.99	3.00	3.01	2.98	3.02
Al	1.92	1.91	1.93	1.93	1.90
Ti	0.02	0.02	0.02	0.01	0.02
Cr	0.01	0.01	0.01	0.02	0.00
Ba	0.00	0.00	0.00	0.00	0.00
Mg	1.66	1.63	1.58	1.66	1.63
Fe	0.97	0.99	0.99	0.98	1.00
Mn	0.04	0.04	0.04	0.04	0.05
Ca	0.39	0.40	0.40	0.40	0.39
Na	0.01	0.01	0.02	0.05	0.02
K	0.00	0.00	0.00	0.01	0.00
Zr	0.00	0.00	0.00	0.00	0.00
SO3	0.00	0.00	0.00	0.00	0.00
Cl	0.00	0.00	0.00	0.00	0.00
F	0.00	0.00	0.00	0.00	0.00
Sum	8.03	8.02	8.01	8.07	8.02

Table 6

	vm_grt6	vm_grt7	vm_grt8	vm_grt9	vm_grt10
wt %					
SiO2	40.93	40.00	40.88	39.46	40.97
TiO2	0.31	0.31	0.36	5.62	0.34
Al2O3	21.79	21.79	22.72	16.11	21.87
Cr2O3	0.27	0.12	0.22	0.14	0.17
BaO	0.00	0.00	0.00	0.00	0.00
FeO	15.97	16.02	15.99	11.25	15.95
MnO	0.69	0.77	0.66	0.33	0.72
MgO	15.08	15.02	14.79	13.60	14.85
CaO	4.78	4.83	4.93	8.05	4.99
Na2O	0.13	0.08	0.11	3.26	0.11
K2O	0.04	0.01	0.00	0.38	0.03
ZrO2	0.00	0.00	0.00	0.00	0.00
SO3	0.00	0.00	0.00	0.00	0.00
Cl	0.00	0.00	0.00	0.00	0.00
F	0.00	0.00	0.00	0.00	0.00
Total	100.00	98.94	100.65	98.19	100.00
Ferrous Form	vm_grt6	vm_grt7	vm_grt8	vm_grt9	vm_grt10
Si	3.02	2.98	2.99	3.00	3.02
Al	1.89	1.92	1.96	1.44	1.90
Ti	0.02	0.02	0.02	0.32	0.02
Cr	0.02	0.01	0.01	0.01	0.01
Ba	0.00	0.00	0.00	0.00	0.00
Mg	1.66	1.67	1.61	1.54	1.63
Fe	0.98	1.00	0.98	0.71	0.98
Mn	0.04	0.05	0.04	0.02	0.04
Ca	0.38	0.39	0.39	0.66	0.39
Na	0.02	0.01	0.02	0.48	0.02
K	0.00	0.00	0.00	0.04	0.00
Zr	0.00	0.00	0.00	0.00	0.00
SO3	0.00	0.00	0.00	0.00	0.00
Cl	0.00	0.00	0.00	0.00	0.00
F	0.00	0.00	0.00	0.00	0.00
Sum	8.02	8.04	8.01	8.22	8.02

Table 7

	vm_bt12	vm_cpx13	vm_grt24
wt %			
SiO2	38.09	52.75	41.21
TiO2	2.66	0.34	0.38
Al2O3	16.96	1.96	22.91
Cr2O3	0.18	0.14	0.14
BaO	0.00	0.00	0.00
FeO	10.75	7.17	15.84
MnO	0.14	0.14	0.65
MgO	18.06	16.75	15.33
CaO	0.02	18.57	4.88
Na2O	0.67	0.68	0.07
K2O	9.34	0.00	0.01
ZrO2	0.00	0.00	0.00
SO3	0.00	0.00	0.00
Cl	0.00	0.00	0.00
F	0.00	0.00	0.00
Total	96.86	98.50	101.43
Ferrous Form	vm_bt12	vm_cpx13	vm_grt24
Si	2.74	1.96	2.99
Al	1.44	0.09	1.96
Ti	0.14	0.01	0.02
Cr	0.01	0.00	0.01
Ba	0.00	0.00	0.00
Mg	1.94	0.93	1.66
Fe	0.65	0.22	0.96
Mn	0.01	0.00	0.04
Ca	0.00	0.74	0.38
Na	0.09	0.05	0.01
K	0.86	0.00	0.00
Zr	0.00	0.00	0.00
SO3	0.00	0.00	0.00
Cl	0.00	0.00	0.00
F	0.00	0.00	0.00
Sum	7.87	4.01	8.02